

AD-A181 963

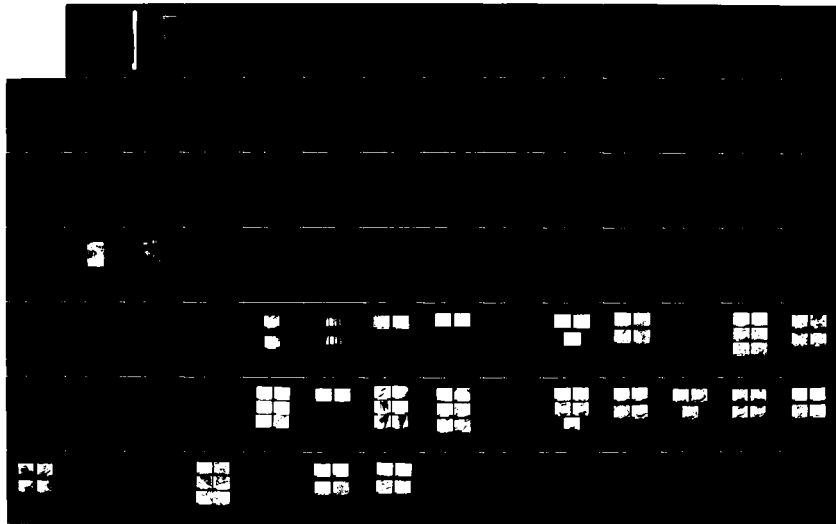
LASER AND ELECTROCHEMICAL STUDIES OF METALLIZATIONS IN
ELECTRONIC DEVICES (U) ISRAEL INST OF METALS HAIFA
J ZAHUT ET AL. JAN 87 EOAD-TR-87-06 AFOSR-85-0309

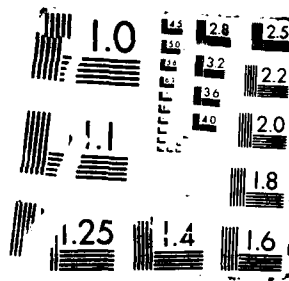
1/2

UNCLASSIFIED

F/C 11/6.1

NL





BOARD-TR-87 061
DTIC FILE COPY

MINISTRY OF INDUSTRY
COMMERCE AND TOURISM
INDUSTRIAL RESEARCH
ADMINISTRATION

משרד התעשייה,
המסחר והתיירות
המחקר
התעשייתי

מכון המחקר הישראלי • ISRAEL INSTITUTE OF METALS



TECHNION
RESEARCH AND
DEVELOPMENT
FOUNDATION LTD.

מוסד
המחקר
למחקר
בע"מ

AD-A181 963

LASER AND ELECTROCHEMICAL STUDIES OF METALLIZATIONS
IN ELECTRONIC DEVICES

First Annual Research Report

No. 504-591

Oct. 85 - Oct. 86

J. Zahavi
M. Rotel

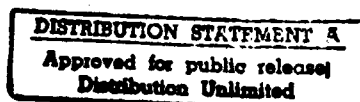
Israel Institute of Metals

B. Dobbs

WPAFB, MLSA, Dayton, Ohio 45433, U.S.A.



Technion City, Haifa, January 1987



87 6 23 065

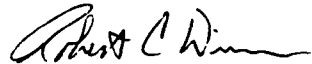
EOARD-TR-87-06

This report has been reviewed by the EOARD Information Office and is releasable to the National Technical Information Service (NTIS). At NTIS it will be releasable to the general public, including foreign nations.

This technical report has been reviewed and is approved for publication.



LARELL K. SMITH, Lt Col, USAF
Chief, Physical Chemistry/Materials



ROBERT C. WINN, Lt Colonel, USAF
Chief Scientist

EOARD-TR-67 061
Technion Research
and Development Foundation

Israel Institute
of Metals

LASER AND ELECTROCHEMICAL STUDIES OF METALLIZATIONS
IN ELECTRONIC DEVICES

First Annual Research Report
No. 504-591
Oct. 85 - Oct. 86

J. Zahavi
M. Rotel

Israel Institute of Metals

B. Dobbs

WPAFB, MLSA, Dayton, Ohio 45433, U.S.A.



Accession For	
NTIS CRA&I	<input checked="" type="checkbox"/>
DTIC TAB	<input type="checkbox"/>
Unannounced	<input type="checkbox"/>
Justification	
By <i>lth on file</i>	
Distribution	
Availability Codes	
Dist	Avail and/or Special
<i>A-1</i>	

Technion City, Haifa, January 1987

Copyright © 1986 , by J. Zahavi, M. Rotel, Israel Institute of
Metals and Technion Research and Development Foundation, Ltd.

UNCLASSIFIED
SECURITY CLASSIFICATION OF THIS PAGE

REPORT DOCUMENTATION PAGE

1a. REPORT SECURITY CLASSIFICATION Unclassified			1b. RESTRICTIVE MARKINGS		
2a. SECURITY CLASSIFICATION AUTHORITY			3. DISTRIBUTION/AVAILABILITY OF REPORT Approved for public release; Distribution unlimited		
2b. DECLASSIFICATION/DOWNGRADING SCHEDULE			5. MONITORING ORGANIZATION REPORT NUMBER(S) EOARD-TR-87-06		
4. PERFORMING ORGANIZATION REPORT NUMBER(S)			7a. NAME OF MONITORING ORGANIZATION European Office of Aerospace Research and Development		
6a. NAME OF PERFORMING ORGANIZATION Technion Research and Development Foundation		6b. OFFICE SYMBOL (If applicable)		7b. ADDRESS (City, State, and ZIP Code) Box 14 FPO New York 09510-0200	
6c. ADDRESS (City, State, and ZIP Code) Israel Institute of Metals Technion City Haifa 32000, Israel			9. PROCUREMENT INSTRUMENT IDENTIFICATION NUMBER AFOSR 85-0309		
8a. NAME OF FUNDING/SPONSORING ORGANIZATION European Office of Aerospace Research & Development		8b. OFFICE SYMBOL (If applicable) LRP		10. SOURCE OF FUNDING NUMBERS	
8c. ADDRESS (City, State, and ZIP Code) Box 14 FPO New York 09510-0200		PROGRAM ELEMENT NO. 61102F		PROJECT NO. 2301	TASK NO. D1
				WORK UNIT ACCESSION NO.	
11. TITLE (Include Security Classification) LASER AND ELECTROCHEMICAL STUDIES OF METALLIZATIONS IN ELECTRONIC DEVICES					
12. PERSONAL AUTHOR(S) J. Zahavi and M. Rotel					
13a. TYPE OF REPORT Final Scientific		13b. TIME COVERED FROM Oct 85 TO Oct 86		14. DATE OF REPORT (Year, Month, Day) 1987 January	
15. PAGE COUNT					
16. SUPPLEMENTARY NOTATION					
17. COSATI CODES			18. SUBJECT TERMS (Continue on reverse if necessary and identify by block number)		
FIELD	GROUP	SUB-GROUP	Tiny Lead, Electrochemical, polarization, Laser, Treatment.		
19. ABSTRACT (Continue on reverse if necessary and identify by block number) Environmental and corrosion behavior of Pb-Sn electrodeposits was studied by electrochemical polarization techniques and SEM. Experiments with D.I. water containing 10^{-3} to 10^{-1} MCL ⁻ showed that for a given deposit, the corrosion rate increases with Cl ⁻ concentration and decreases with deposit thickness in the 2-50μm range. The mode of corrosion was associated with preferred dissolution of lead. Deposits were also irradiated with Nd-Yag pulse laser at 530nm and 2×10^8 - 2×10^9 watt/cm ² power density and the treated zones were examined.					
20. DISTRIBUTION/AVAILABILITY OF ABSTRACT <input checked="" type="checkbox"/> UNCLASSIFIED/UNLIMITED <input type="checkbox"/> SAME AS RPT. <input type="checkbox"/> DTIC USERS			21. ABSTRACT SECURITY CLASSIFICATION Unclassified		
22a. NAME OF RESPONSIBLE INDIVIDUAL LARELL K. SMITH, Lt Col, USAF			22b. TELEPHONE (Include Area Code) (44 1) 409-4505		22c. OFFICE SYMBOL EOARD/LRP

DD FORM 1473, 84 MAR

83 APR edition may be used until exhausted.
All other editions are obsolete.

SECURITY CLASSIFICATION OF THIS PAGE

CONTENTS

	<u>Page</u>
1. INTRODUCTION	9
2. BACKGROUND	10
2.1 Laser Applications	10
2.1.1 General	10
2.1.2 Interaction laser-material - heating and cooling process	10
2.2 Pb-Sn metallurgy	14
2.2.1 Pb-Sn phase diagram	14
2.2.2 Pb-Sn surface composition	16
2.3 Corrosion	17
2.3.1 Polarization	17
2.3.1.1 Polarization theory	17
2.3.1.1a Tafel Plot Technique	18
2.3.1.1b Calculation of corrosion rate	22
2.3.2 Corrosion behavior of lead and lead alloys	24
2.3.3 Corrosion behavior of tin and tin alloys ...	27
2.3.4 Corrosion behavior of tin and lead alloys - solders	29
3. EXPERIMENTAL	31
3.1 Electroplating	31
3.1.1 Laboratory electroplating	31
3.1.1.1 Specimen preparation and pretreatment	31
3.1.1.2 Electroplating bath	32
3.1.1.3 Electroplating solutions	33

3.1.1.3A Tin-lead alloy plating solution ...	33
3.1.1.3B Fluoroboric acid solution	33
3.1.1.3C Bichromate acid solution	33
3.1.1.4 Electroplating calculation	33
3.1.1.4A Current density	33
3.1.1.4B Coating thickness	33
3.2 Laser operation	34
3.2.1 Laser energy calculations	34
3.3 Polarization	36
3.3.1 Polarization set-up	36
3.3.1.1 Corrosion measuring	36
3.3.1.2 Experimental procedure	40
3.4 Mode of Analysis	41
4. RESULTS	42
4.1 Polarization-corrosion resistance tests	42
4.1.1 Preliminary experiments	42
4.1.2 Polarization of laboratory electroplating samples	43
4.2 SEM observations after polarization	54
4.2.1 Commercial specimens	54
4.2.2 Laboratory specimens	59
4.3 Laser treatment	67
4.3.1 Laser experiments - lines	67
4.3.2 Laser experiments - spots	73
4.3.3 Laser experiments - Area	81
4.3.4 Laser experiments - defocus experiments	83
4.3.5 Auger spectroscopy observations of laser treated area	86
4.3.6 X-ray diffraction of laser treated area	86

5. DISCUSSION	92
5.1 Corrosion of Pb-Sn alloy	92
5.1.1 Polarization curves	92
5.1.2 Effect of chloride concentration	92
5.1.3 Effect of heat treatment on the corrosion resistance	93
5.1.4 Effect of coating thickness on corrosion resistance	93
5.1.5 Corrosion mode	94
5.2 Effect of heat treatment on the metallurgy of Pb-Sn alloy coating	95
5.3 Effect of laser treatment on the surface of Pb-Sn alloy	96
5.4 Selecting laser conditions	96
5.5 Further research	97
6. CONCLUSIONS	98
7. REFERENCES	99

FIGURE CAPTIONS

Fig. 2.1	Schematic intensity and temperature profiles..	12
Fig. 2.2	Pb-Sn phase diagram	15
Fig. 2.3	Cu-Sn phase diagram	15
Fig. 2.4	Tafel plot	19
Fig. 2.5	Response of a reduction-oxidation system to an externally applied potential	19
Fig. 2.6	Measured current as a function of externally applied potential	21
Fig. 2.7	Potential-current relationship for a mixed electrode system consisting of two electrochemical reactions	23
Fig. 2.8	Effect of mixed electrode system concentration and resistance effects on the measured current as a function of potential	23
Fig. 2.9	Relationship between weight loss or weight gain and time for lead immersed in various environments	26
Fig. 2.10	Potential/PH diagram for the Pb-H ₂ O system .	28
Fig. 2.11	Potential/PH diagram for tin	28
Fig. 2.12	Lead and tin in the galvanic series	30
Fig. 3.1	Electroplating bath	32
Fig. 3.2	Schematic description of the laser working system	35
Fig. 3.3	General description of the corrosion measurement system	38
Fig. 3.4	Detailed description of the corrosion cell system	39
Fig. 4.1	Typical potentiodynamic curves obtained for Pb/Sn commercial specimen	45
Fig. 4.2	Effect of chloride concentration on Pb-Sn corrosion rate	46
Fig. 4.3	Typical polarization curves obtained during potentiodynamic polarization of Pb-Sn specimen with various coating thickness at 10 ⁻² M NaCl	48
Fig. 4.4	Typical polarization curves obtained during potentiodynamic polarization of Pb-Sn specimen after melting with various coating thickness at 10 ⁻² M Cl ⁻	49

Fig. 4.5	Typical potentiodynamic curves obtained during potentiodynamic polarization of Pb-Sn coating at 10^{-3}M Cl^-	50
Fig. 4.6	Corrosion rates of Pb-Sn coating versus coating thickness	53
Fig. 4.7	Surface SEM observations of commercial Pb-Sn 40/60 deposits on epoxy plated copper ..	55
Fig. 4.8	E.D.S. results of areas shown in Fig. 4.7.....	56
Fig. 4.9	Surface SEM observations of commercial Pb-Sn Deposits after polarization	57
Fig. 4.10	Surface SEM observations of commercial Pb-Sn 40/60 deposited on epoxy plated 70 μm copper	58
Fig. 4.11	SEM observations of corroded areas after potentiodynamic polarization at 10^{-2}M NaCl of specimen with various Pb-Sn coating thickness	60
Fig. 4.12	SEM observations of corroded and uncorroded surfaces of specimen with various Pb-Sn coating thickness after polarization in 10^{-2}M NaCl	61
Fig. 4.13	E.D.S. microanalysis of corroded and uncorroded specimen of various thickness	62
Fig. 4.14	SEM observations of heat treated specimen before and after potentiodynamic polarization 10^{-2} M NaCl at various thickness	63
Fig. 4.15	SEM observations of heat treated specimen before and after potentiodynamic polarization in 10^{-2} M NaCl at various thickness	64
Fig. 4.16	The effect of polarization on lead concentration for various coating thickness	66
Fig. 4.17	SEM observations of laser treated surfaces at various laser pulse power densities	69
Fig. 4.18	SEM observations of 6.8 μm Pb-Sn coating on copper foil	70
Fig. 4.19	SEM observations of lines formed by laser treatment on 2.7 μm Pb-Sn coating	71
Fig. 4.20	Enlargement of the area shown in Fig. 4.20	72
Fig. 4.21	SEM observations of one pulse irradiation at various power densities. Deposit thickness 6 μm	74

Fig. 4.22	SEM observations of the effect of laser number of pulses at constant pulse intensities	75
Fig. 4.23	SEM observations of the effect of laser number of pulses at constant pulse intensities	76
Fig. 4.24	SEM observations of the effect of laser number of pulses at constant pulse intensities	77
Fig. 4.25	SEM observations of the effect of laser number pulses, laser energy per pulse 0.25 watt/cm ²	78
Fig. 4.26	SEM observations of effect of pulses and power density	79
Fig. 4.27	Laser affected area's diameter as affected by the laser density	80
Fig. 4.28	SEM observations of area formed on 5.5μm Pb-Sn coating of copper foil	82
Fig. 4.29	SEM observations of defocus laser experiments	84
Fig. 4.30	SEM observations of area formed at defocus laser experiments	85
Fig. 4.31	Auger spectroscopy observations of Pb-Sn coating	87
Fig. 4.32	Auger spectroscopy observations of laser treated area of Pb-Sn coating	88
Fig. 4.33	X-ray diffraction of Pb-Sn coating (2.7μm on copper foil)	89
Fig. 5.1	Schematic description of corrosion mode of Pb-Sn as deposited specimen	94
Fig. 5.2	Schematic description of corrosion mode of heat treated Pb-Sn alloy coating	95

TABLE CAPTIONS

Table 2.1	Various commercial lasers	11
Table 2.2	Compounds of lead	25
Table 4.1	Results of preliminary potentiodynamic polarization of commercial specimens	47
Table 4.2a	Summary of potentiodynamic polarization tests at 10^{-2} M or NaCl with nitrogen purging - as deposited	51
Table 4.2b	Summary of corrosion test at 10^{-2} M NaCl after melting in oven	51
Table 4.3a	Corrosion test results at 10^{-2} M NaCl with nitrogen purging - as coated specimen	52
Table 4.3b	Corrosion tests results at 10^{-2} M NaCl with nitrogen purging - specimen after melting in oven at 300°C	52
Table 4.4	Summary of E.D.S. analysis of laboratory specimen before and after polarization	65
Table 4.5	E.D.S. microanalysis of laser treated zone with various laser intensities	68
Table 4.6	Summary of the E.D.S. results obtained during producing laser treatment area on Pb-Sn coating	81
Table 4.7	E.D.S. results of the various areas shown in Fig. 4.30	83
Table 4.8	X-ray diffraction of Pb-Sn coating	90

1. INTRODUCTION

In recent years laser technology has developed and is used in many industrial processes. Pulse lasers with very short pulse duration are used to heat the surface layer so rapidly that the bulk temperature is not affected. In this research, work is done in order to produce laser-treated area of Pb-Sn alloy coating on copper foil in order to obtain an efficient process for the microelectronics and electronics industry.

Corrosion behavior of Pb-Sn alloy before and after heat treatment was investigated, using the potentiodynamic polarization technique.

2. BACKGROUND

2.1 Laser Application

2.2.1 General

Laser is a unique source of radiation capable of delivering intense coherent electromagnetic field in the spectral range between the ultraviolet and the far infrared. Lasers can be continuous or pulsed with a pulse duration as short as a fraction of picosend. Output power of the laser can reach very high energy levels. Table 2.1 summarized the various kinds of commercial laser available and their output power.

Lasers are used for material processing for such applications such as welding, drilling and various forms of micromachinery. In our work, lasers had been used as a point source of energy in order to produce heat treatment of the Pb-Sn coating, on copper that can be used in the microelectronics for limited small area applications without causing the heating of the adjusted area due to the pulse laser beam properties: very short pulse duration (9 nsec) and a beam that can be aimed and focused on previous determined area.

2.1.2 Interaction Laser-Material-Heating and Cooling Process

Thermal considerations are very important where laser beams are used in material processing. Fig. 2.1 is an approximated schematic representation of intensity and temperature profiles produced by laser beam. Laser beam with pulse duration (t_p) at constant and uniform intensity I (watt/cm²) normally incident on a plane boundary of an absorbing material with an absorption coefficient α . The reflection coefficient at the surface is R . R and α characterize the optical properties of the material and are assumed to be independent of temperature. The thermal properties of the material are described by the specific heat per unit mass C_v , the mass density ρ and the thermal conductivity k . The heat diffusivity $D = K/C_v\rho$ determines a characteristics length $(2Dt)^{1/2}$, which indicates how much the temperature profile is spread out during the laser pulse. There are two limiting cases which are illustrated in Figs. 2.1a and 2.1b.

Table 2.1: Various Common Lasers

Laser	Wave length μm	Operation mode	Maximum power Watt	
			Pulse	Average
Solid state laser				
Ruby	0.694	pulse	10^{10}	
Na^{+3} /glass	1.064	pulse	10^{12}	
Na^{+3} /YAG	1.064	pulse, CW	10^{12}	10^6
Semi-conductor lasers				
GaAs	0.85	pulse, CW	10^2	10^{-2}
Gas Lasers				
He-Ne	0.633			
	1.152	CW	10^{-2}	
	3.391			
Ne^{+}	0.332			
Ar^{+}	0.488; 0.515	CW	0.1-10	
Kr^{+}	0.568; 0.647			
Xe^{+}	0.526; 0.547			
He-Cd	0.352; 0.442	CW	10^{-1}	
Cu CuX	0.511	CW	10^{-4}	10^{-1}
N_2	0.337	CW	10^6	1
CO_2	10.6	pulse, CW	10^{10}	1000
Xe	0.17	CW	10^9	
ArF	0.248	pulse	10^{10}	
KrF	0.193	pulse	10^{10}	

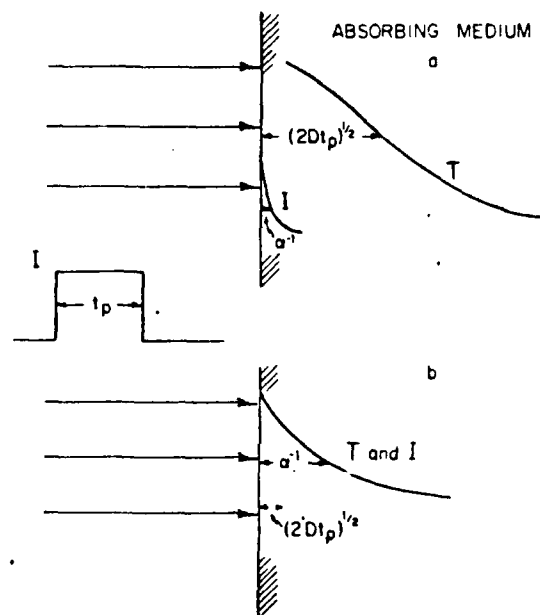


Fig. 2.1 Schematic Intensity and Temperature Profiles.

- a. The penetration depth α^{-1} of the light is small compared to the thermal diffusion length $(2Dt_p)^{1/2}$.
- b. The penetration depth of the light is large compared to the thermal diffusion length.

Case a: The optical absorption depth α^{-1} is small compared to thermal diffusion length, $\alpha(2Dt_p)^{1/2} \gg 1$. In this case, the energy absorbed during the laser pulse $(1-R)It_p$ is used to heat a layer of thickness $(2Dt)^{1/2}$. The average temperature rise in this layer is

$$\Delta T = (1-R)I t_p / c_v (2Dt_p)^{1/2}$$

After the laser pulse the heat in this layer diffuses into the substrate. The order of magnitude of the cooling time is again equal to t_p , the time it takes the heat to diffuse over a distance. Thus both the heating and cooling have the order of magnitude.

$$\frac{\Delta T}{t_p} = (1-R)I / c_v (2Dt_p)^{1/2}$$

Case b: The optical absorption α^{-1} is large compared to the thermal diffusion length, $(2Dt)^{1/2} \gg 1$. The light absorption creates an exponential temperature profile with characteristic length α^{-1} .

$$\Delta T(z) = (1-R)\alpha I e^{-\alpha z} t_p / c_v \rho$$

The heating rate is $\Delta T(z)/t_p$. The cooling rate determines the structure of the surface layer after the laser treatment. Since the heat has to diffuse into a the substrate over a length α^{-1} , the cooling time is roughly $\alpha^{-2}/2D$. The cooling rate has the order of magnitude

$$\frac{dT}{dt} = (1-R)\alpha^3 (2Dt_p / c_v \rho)$$

From an experimental point of view, the laser pulses can always be given sufficient energy to evaporate the surface. Thus the maximum temperature rise is limited by the boiling point of the material. For practical heat treating purposes, one would not wish to exceed the melting temperature T_m very much. Taking, therefore, $\Delta T = T_m$, it is evident that the faster cooling rates pertain in case a. Most of the cases of practical interest are of case a, thus the cooling rate T_m/t_p are in layers of $(2Dt_p)^{1/2}$.

Appendix A shows calculations made according to case a for copper and lead. More accurate and complex analysis can be found in the literature [10,11,12]. The importance of this calculation is to give an approximation of the energy needed to produce melting of Pb by pulse laser.

2.2 Pb-Sn Metallurgy

Pb-Sn alloys are used in the electronic industry as a soft soldering material. Soft soldering process is producing an intermediate layer between the base metal and other materials. The connected metals do not melt during this process only the solder is melted and bridges the distance between the metals. Most of the soldering alloys are melted below 300°C. In this work, the use of Pb-Sn alloy for printed circuits boards was investigated. The Pb-Sn is electrodeposited on copper conductive line and used as a coverage for the copper in the etching process and as soft soldering material for further contacts. In order to improve the solderability of the electrodeposited Pb-Sn alloy a reflow process is applied. In this process, the prepared printed circuit board is heated in order to melt the Pb-Sn. The solidified alloy shows better properties than the electrodeposited alloy.

- A. Brighter and smoother surfaces.
- B. Higher solderability.
- C. It is believed that impurities present at the bulk materials moved to the surface.
- D. Improved adhesion between the copper and the electrodeposited Pb-Sn.

2.2.1 Pb-Sn Phase Diagram

Fig. 2.2 shows the tin-lead phase diagram. This is a simple eutectic binary system. The eutectic point is in 61.9% Sn (wt %) and the melting point is 183.2°C. For most applications in the electronic industry the eutectic composition is used in order to reduce the temperature needed for soldering and to minimize the pasty range.

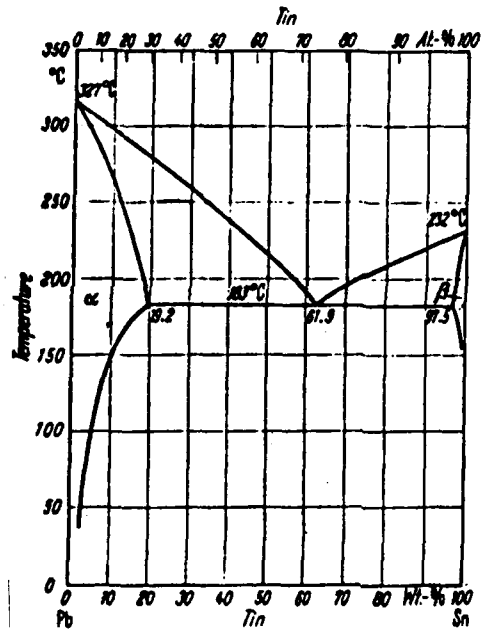


Fig. 2.2: Tin-lead phase diagram (8)

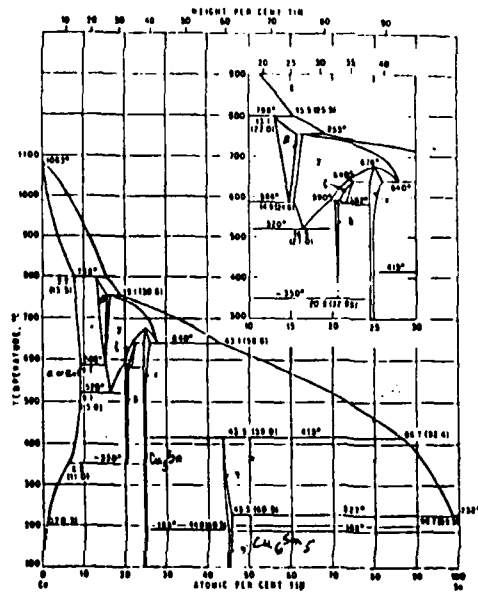


Fig. 2.3: Cu-Sn phase diagram

Because the eutectic composition is 61.9%Sn and 38.1% Pb all the lead base alloys in the system contain primary grains of lead-rich solid solution. Alloys that contained more than 19% tin contain eutectic, which consists of lead rich solid solution in a tin rich matrix. A high rate of solidification, as in most soldering applications, favors the globular type of eutectic [7].

Although the solubility of tin in lead at the eutectic temperature is 19%; at room temperature, it is reduced to about 2% causing considerable precipitation of tin rich solid solution which appears as granules and needles with the grains of lead-rich solid solution[7].

The Pb-Sn soldering material that wets the base metal usually produces a layer of intermetallic compounds between the soldering material and the base metal. Intermetallic phases between copper and tin are known. Fig. 2.3 shows the phase diagram of Cu-Sn and the zones in which the intermetallic compound Cu_3Sn and Cu_6Sn_5 are produced. Cu_3Sn is produced only when the melt's temperature was higher than 415°, but Cu_6Sn_5 are recrystallized at lower temperature.

2.2.2 Pb-Sn Surface Composition

R.J. Bird [8] examined lead-indium and lead-tin alloys by ESCA spectroscopy. He found that tin and indium are markedly segregated at the surfaces in oxidized form. The alloying elements additionally promote the formation of a form of lead (thought to be PbO_2) more highly oxidized than that obtained on the surface of pure lead under the same conditions.

R.P. Frandenthal and D.J. Siconolfi [9] show by Auger electron spectroscopy studies that lead segregates to the surface of the Sn-rich alloy at all temperatures studied, while tin segregates to the surface of Pb-rich alloy at temperature below 180°C.

2.3 Corrosion

2.3.1 Polarization

Potentiodynamic polarization is the characterization of metal specimens by its current-potential relationship. The specimen is forced to act as an anode such that it corrodes or forms oxide coating. The potentiodynamic polarization is used to determine corrosion characteristics of metal specimen in the environment of interest.

2.3.1.1 Polarization Theory

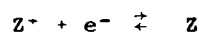
When a metal specimen is immersed in a corrosive medium, both reduction and oxidation processes occur on its surface. Typically the specimen oxidized (corrodes) and the medium (solvent) is reduced (liberation of hydrogen). The specimen must function as both anode and cathode and both cathodic and anodic currents occur on the specimen surface. A specimen in contact with a corrosive liquid assumes a potential relative to a reference electrode termed the corrosion potential, E_{corr} . A specimen at E_{corr} has equal anodic and cathodic currents on its surface, so there is no net current to be measured. E_{corr} can be defined as the potential at which the rate of oxidation is exactly equal to the rate of reduction. If the specimen is polarized in the positive direction the cathodic component becomes negligible with respect to the anodic component. If the specimen is polarized in the negative direction, the cathodic current predominated and the anodic component becomes negligible.

Experimentally, one measures polarization characteristics by plotting the current response as a function of the applied potential on semi-log chart, where cathodic potentials are negative with respect to E_{corr} and anodic potentials are positive with respect to E_{corr} (Fig. 4.1 shows experimentally polarization curves).

2.3.1.1 A Tafel Plot Technique

Where the potentiodynamic polarization technique is suited to giving an overall view of the corrosion behavior of a material, the Tafel technique focuses on the problem of accurately determining the corrosion rate of a material. When the potential-current function is plotted on semi-log paper, for a few hundred millivolts near E_{corr} , it characteristically exhibits a linear region. The slopes of this region are known as Tafel constants and their projection at the intersection with E_{corr} defines i_{corr} and thus the corrosion rate (Fig. 2.4). Another technique to define corrosion rate is to use the Tafel constants in the polarization Resistance Plot.

In a simple n-corroding system containing Z and Z^+ at equilibrium



and

$$i_{r,z} = i_{o,z} = i_{ex}$$

where

$i_{r,z}$ = current for reduction of Z^+

$i_{o,z}$ = current for oxidation of Z

i_{ex} = the exchange current.

If a potential is imposed on the metal from an external voltage source the reaction rate is controlled by a slow chemical step that requires an activation energy

$$i_{r,z} = i_{ex} e^{-\eta/\beta'}$$

$$i_{o,z} = i_{ex} e^{-\eta/\beta''}$$

where η = the over-voltage, the difference between the potential imposed on the specimen and the corrosion potential ($\eta = E_{\text{app}} - E_{\text{corr}}$) and where β' and β'' are constants.

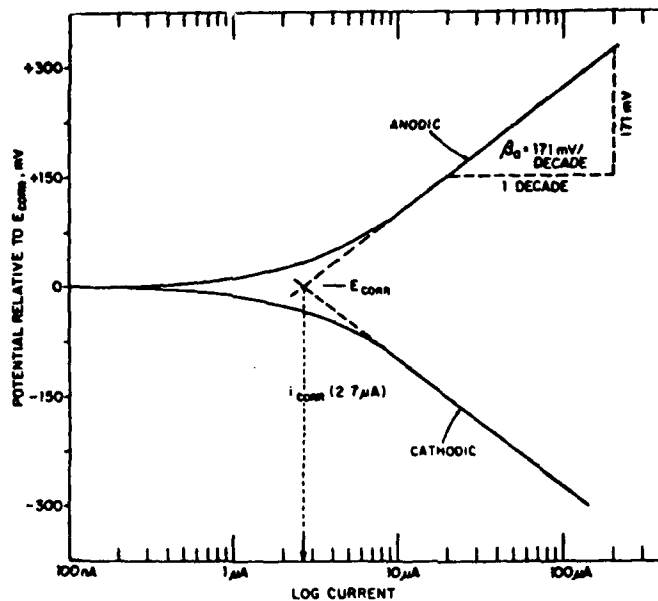


Fig. 2.4: Tafel plot

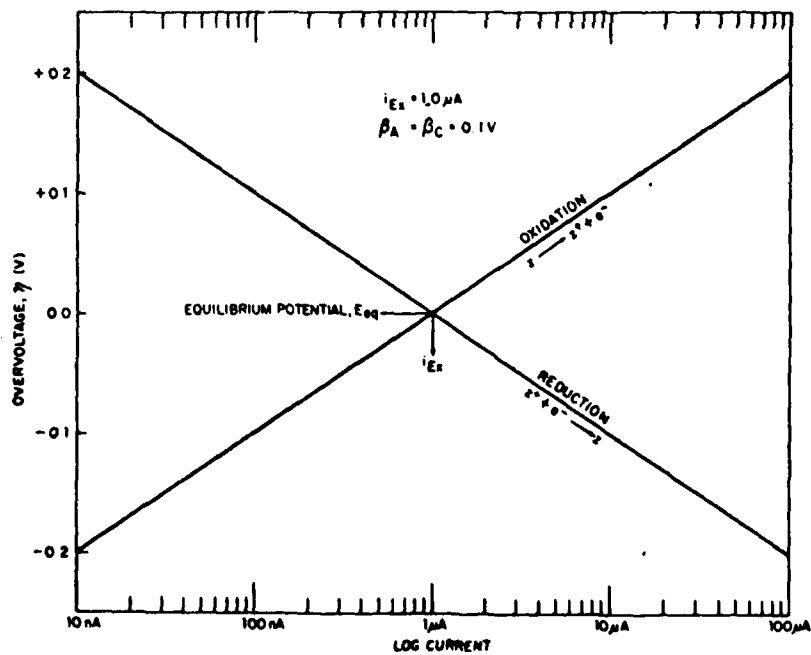


Fig. 2.5: Response of a reduction-oxidation system to an externally applied potential

Taking of the log of the above equations and solving for η yields

$$\eta = -\beta_o \log$$

$$\eta = \beta_a \log$$

where, $\beta_o = 2.3\beta'$ and $\beta_a = 2.3\beta''$. These are called Tafel Constants.

Fig. 2.5 is a theoretical drawing of these relationships assuming $i_{ax} = 1\mu A$ and β_o and $\beta_a = 0.1V$.

Experimentally, only the total current is measured. The total current is the difference between the rate of oxidation and the rate of reduction.

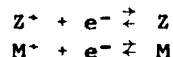
$$i_{meas} = i_{r,z} - i_{o,z}$$

so

$$\eta = -\beta_o \log \frac{i_{meas} + i_{o,z}}{i_{Ex}}$$

A plot η vs. $\log i_{meas}$ is shown in Fig. 2.6.

In corroding system the corroding metal must also be considered and these two systems are to be treated:



Each of these systems has its own equilibrium potential exchange current and Tafel slope. At the corrosion potential

$$i_{r,z} + i_{r,M} = i_{o,z} + i_{o,M}$$

Fig. 2.7 illustrated the potential current relationship for such a mixed-electrode system. When E_{corr} of the mixed-electrode system is sufficiently different from the equilibrium potentials of the individual reactions $i_{r,M}$ and $i_{o,z}$ become insignificant in comparison to $i_{o,M}$ and $i_{r,z}$, respectively. The corrosion rate becomes equal to $i_{o,M}$ or $i_{r,z}$. The corrosion potential is closely approximated by the potential at which $i_{r,z} = i_{o,M}$.

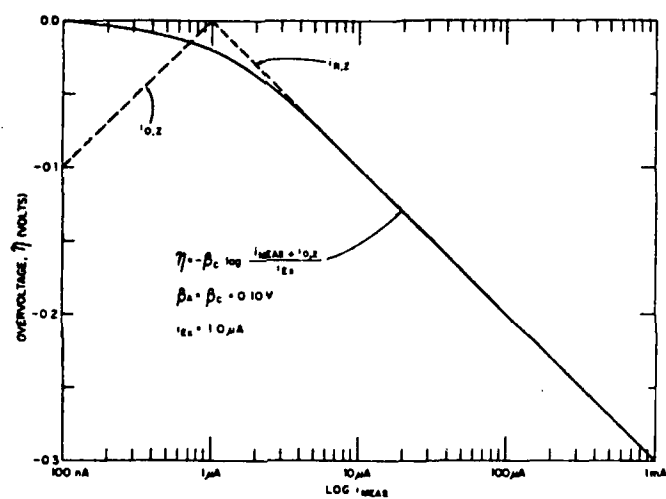


Fig. 2.6: Measured current as a function of externally applied potential

The overall effect of the mixed electrode system, concentration polarization and resistance effects is shown in Fig. 2.8. Concentration polarization occurs when the reaction rate is so high, that the electroactive species cannot reach or be removed from the electrode surface at a sufficiently rapid rate. The reaction rate became diffusion control. As increases the current becomes diffusion limited and the linear current range is truncated. The effect of concentration polarization is minimized by stirring the solution.

2.3.1.1b Calculation of Corrosion Rate from the Corrosion Current

According to Faraday's Law

$$Q = \frac{nFW}{M}$$

where

Q = Coulombs

n = number of electrons involved in the electro-chemical reaction

F = the Faraday, 96,487 coulombs

W = weight of electroactive species

M = molecular weight of electroactive species

From Faraday's Law

$$W = QM/nF$$

Since equivalent weight = M/n

$$W = \frac{Q \times E \cdot W}{F}$$

and since $Q = it$ from Faraday's Law

$$W = \frac{it(E \cdot W)}{F}$$

Rearranging gives

$$W/t = \frac{i(E \cdot W)}{F}$$

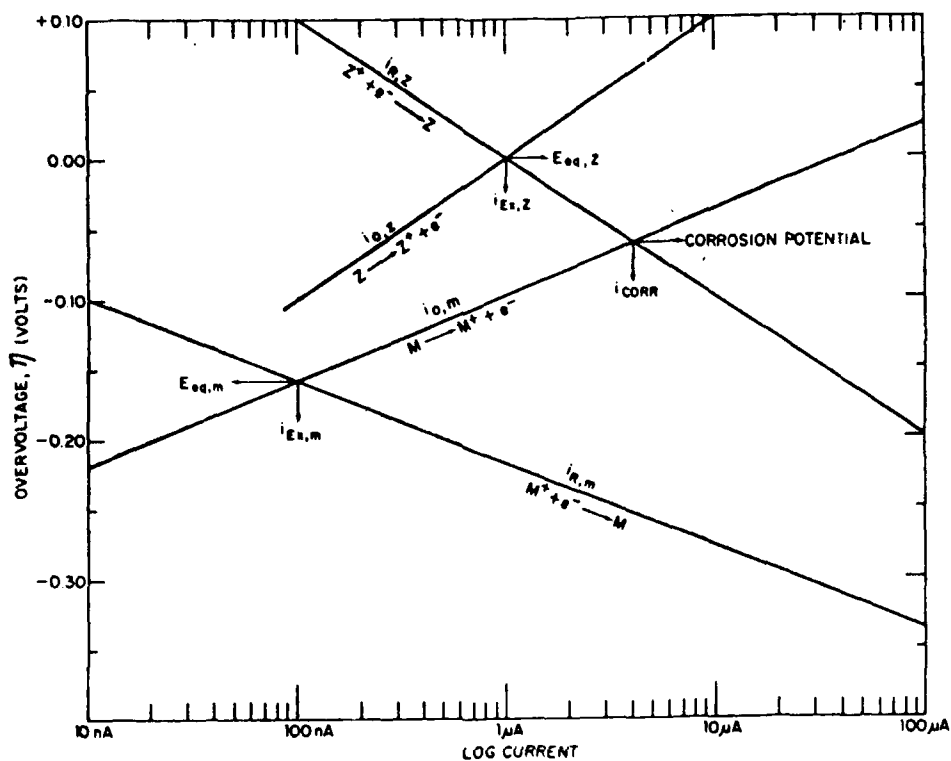


Fig. 2.7: Potential-current relationship for a mixed electrode system consisting of two electrochemical reactions

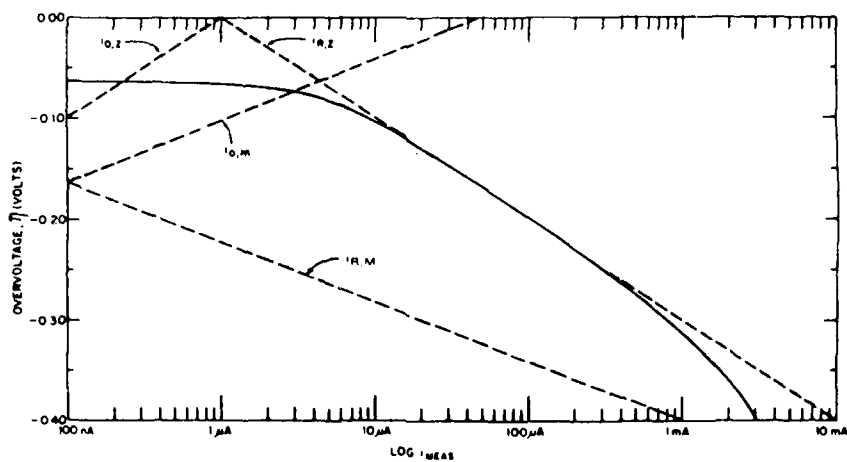


Fig. 2.8: Effect of mixed electrode system, concentration polarization and resistance effects on the measured current as a function of potential.

W/t is the corrosion rate (C.R.) in grams/second. It is convenient and traditional to express corrosion rate as milli-inches per year (mpy). These units provide an indication of penetration.

Dividing the above equation by the electrode area and the density gives

$$C.R. (cm/sec) = i(E.W.)/dFA$$

after converting seconds to years, centimeters to milli-inches, and the Faraday (amp-sec/eq) to microamps, this becomes

$$C.R. (mpy) = \frac{i(E.W.) \times 31.6 \times 10^6 \times 10^3}{dFA \times 2.5 \times 10^6}$$

Expressing the terms i/A as current density and combining all the constants gives:

$$\text{Corrosion Rate (mpy)} = \frac{0.13 I_{corr}(E.W.)}{d}$$

where

I_{corr} = Corrosion current density, $\mu A/cm^2$
 $E.W.$ = Equivalent weight at the corroding species, g
 d = Density of the corroding species, g/cm^3

This equation is used to calculate the corrosion rate directly from I_{corr} .

2.3.2 Corrosion Behavior of Lead and Lead Alloys (2)

The standard electrode potential $E_{Pb^{2+}/Pb} = -0.126V$ show that lead is thermodynamically unstable in acid solutions but stable in neutral solutions. The exchange current for hydrogen reaction on lead is very small ($\times 10^{-12}$ - 10^{-11} A/cm^2), but control of corrosion is usually due to mechanical passivation of the local anodes of the corrosion cells as the majority of lead salts are insoluble and frequently form protective coating or films. Table 2.2 show some of the lead compounds and their solubility products.

Table 2.2: Compounds of Lead (2)

Compound of lead	Formula	Stability product at 25°C	Colour
Acetate	$(\text{CH}_3\text{COO})_2\text{Pb}$	soluble (55 g/100ml)	white
Bromide	PbBr_2	5.7×10^{-6}	white
Carbonate	PbCO_3	3.3×10^{-14}	white
Basic Carbonate	$2\text{PbCO}_3 \cdot \text{Pb}(\text{OH})_2$	as above	white
Chloride	PbCl_2	1×10^{-4}	white
Chromate	PbCrO_4	1.8×10^{-14}	orange
Dioxide	PbO_2	insoluble	black or dark brown
Fluoride	PbF_2	3.7×10^{-8}	white
Hydroxide	$\text{Pb}(\text{OH})_2$	4×10^{-15}	white
Iodide	PbI_2	1.4×10^{-8}	yellow
Monoxide	PbO	insoluble	yellow-red
Nitrate	$\text{Pb}(\text{NO}_3)_2$	soluble (60 g/100ml)	white
Phosphate	$\text{Pb}_3(\text{PO}_4)_2$	10^{-55}	white
Sulphate	PbSO_4	1×10^{-8}	white
Sulphide	PbS	3.4×10^{-28}	black
Triplumbic- tetroxide	Pb_3O_4	insoluble	red

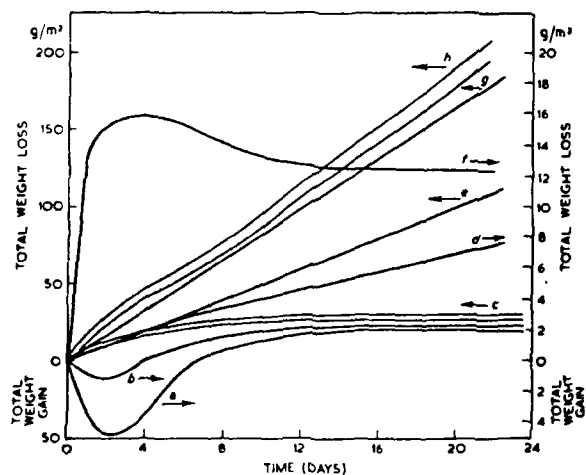


Fig. 2.9 Relationship between weight loss or weight gain and time for lead immersion in various environments (selected from Reference 35).

- | | |
|--|---|
| a 0.5 N $(\text{NH}_4)_2\text{SO}_4$, pH 2.9 | f 0.25 N NaF, pH 6.3 |
| b 0.5 N Na_2SO_4 , pH 5.4 | g 0.5 N $\text{CH}_3\text{COONH}_4 + \text{CH}_3\text{COOH}$, pH 4.6 |
| c 0.01 N NaOH, pH 12.8 | h 0.04 N $\text{Ca}(\text{OH})_2$, pH 13 |
| d 0.01 N $\text{Ba}(\text{OH})_2$, pH 11.9 | 0.5 N CH_3COONa , pH 16 |
| e 0.5 N NaCl, pH 4.9 | 0.5 N $\text{Ba}(\text{OH})_2$, pH > 13 |
| f 0.5 N $\text{CH}_3\text{COONH}_4 + \text{NaOH}$, pH 8.9 | |

Lead is not generally attacked rapidly by salt solutions. The action of nitrates and salts such as potassium and sodium chloride may be rapid. In potassium chloride the corrosion rate increases with concentration to a maximum in 0.05M solution, decrease with higher concentration, and increase again in 2M solution. Only loosely adherent deposits are formed. Fig. 2.9 shows the behavior of lead in various salts.

The potential/pH diagram shown in Fig. 2.10 for the Pb-H₂O system revealed that in the low and high pH corrosion occurs owing to the amphoteric nature of lead. When insoluble salts are involved in the system like in the pH-H₂O-SO₄ system the potential/pH diagram is changed and the corrosion zone in the region of low pH no longer exists owing to thermodynamic stability of PbSO₄.

2.3.3 Corrosion Behavior Tin and Tin Alloys (3)

Pourbaix diagram for tin (Fig. 2.11) refers only to solutions in which formation of soluble tin complexes or protective layers of insoluble salts does not occur. The wide field of stability of the two oxides some of it extending below the field of stability of water indicates easy passivation over a large range of pH, but in either strongly acid or strongly alkaline solutions tin may be dissolved. The standard electrode potential

$E_{\text{Sn}^{2+}/\text{Sn}} = -0.136$. Pure tin is completely resistant to distilled water. Local corrosion occurs in salt solutions which do not form insoluble compounds with stannous ions (e.g., in chloride, bromide, sulphate, nitrate) but is unlikely in solution giving stable precipitates (e.g., borate, mono-hydrogen phosphate, bicarbonate, iodide). In all solutions, oxide film growth occurs and the potential of the metal rises. Contacts with a more noble metal such as copper or nickel increase the number and intensity of pits. Tin when made anodic shows passive behavior as surface films are built up but slow dissolution of tin may persist in some solution and transpassive dissolution may occur in strongly alkaline solution.

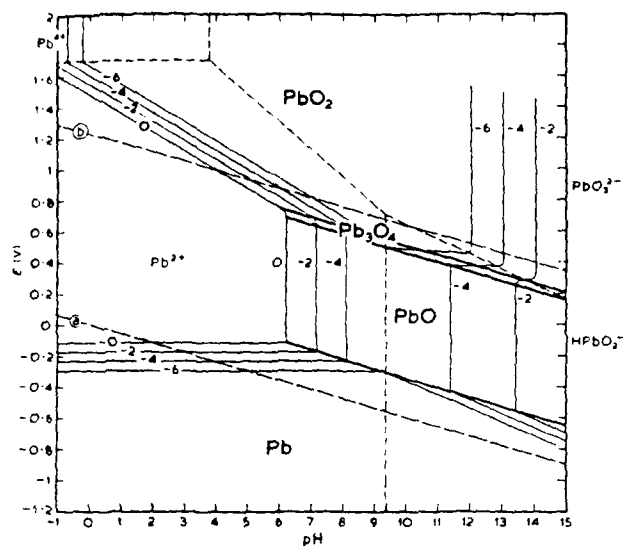


Fig 2. 10 Potential pH diagram for the Pb-H₂O system. The area between (a) and (b) corresponds to the thermodynamic stability of water. Light lines represent equilibrium conditions between a solid phase and an ion at activities 1, 10⁻², 10⁻⁴ and 10⁻⁶. Heavy lines represent equilibrium conditions between two solid phases. Broken lines represent equilibrium conditions between two ions for a ratio of these ions equal to unity (after Delahay, Pourbaix and van Rysseberghe¹¹).

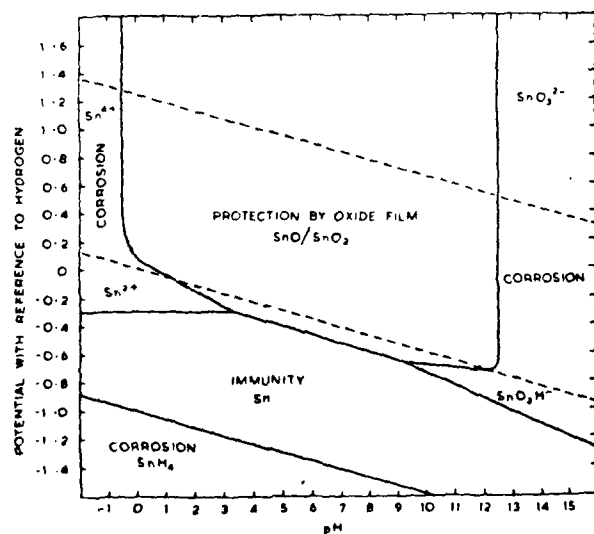


Fig 2. 11 Potential pH diagram for tin. The full lines enclose the zones where the stability of various compounds or ions makes the indicated action possible. The broken lines indicate the limits of stability of water at a pressure of 1 atm (after Reference 4 and Cebalcor).

2.3.4 Corrosion Behavior of Tin and Lead Alloys-Solders

From the literature it is known that solders are anodic to copper (Fig. 2.12). For environment in which tin is less readily corroded than lead, corrosion resistance of the alloy decreases as the lead content increases, the decrease may in some circumstances, be sharp at a particular composition. In the more corrosive media, such as nitride solution, a sharp increase of corrosion rate is observed as the lead content increases beyond 30%. In water with low contents of dissolved salts the corrosion rate increases slowly with lead content up to about 70% and then rises more steeply, but in general run of water supply, the ability of lead to form protective insoluble anodic products is helpful to the durability of solder [2,3].

It was found that in alkaline solutions [6] and in acid solutions [5] the rate of alloy corrosion decrease with increasing tin content in the alloy. A.A. Abdul Azim [4] show that in natural alkaline medium the highest corrosion resistance is provided by solder possessing the eutectic composition.

Laser treatment as a heat treatment can produce higher amounts of eutectic composition in the Pb-Sn alloy coating and thus improve its corrosion resistance. It was interesting to test these results in dilute chloride environment which cause many failures in the microelectronics devices.

Production of intermetallic compounds due to heat treatment between Sn and Cu such as Cu_6Sn_5 can produce better adhesion of the Pb-Sn layer, and it can be tested by diffraction analysis.

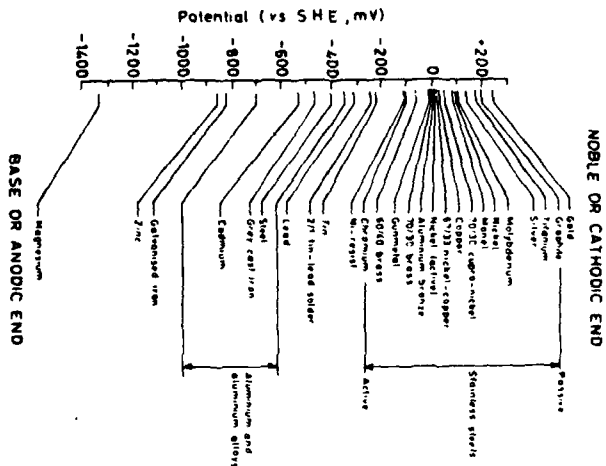


Fig. 21.1 Practical galvanic series of metals and alloys showing potentials on the hydrogen scale (Note that the potentials shown are typical values that will vary according to the nature of the solution) (After Butler, G. and Lyon, H. C. K. *Corrosion and its Prevention in Water*, Leonard Hill, London (1966))

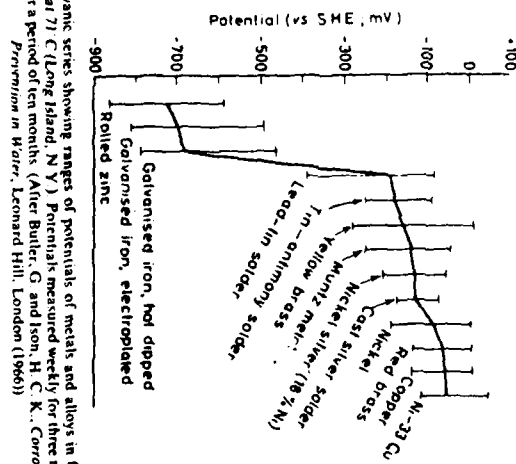


Fig. 21.2 Galvanic series showing ranges of potentials of metals and alloys in flowing hot domestic water at 77°C (Long Island, N.Y.) Potentials measured weekly for three months and then monthly for a period of ten months (After Butler, G. and Lyon, H. C. K. *Corrosion and its Prevention in Water*, Leonard Hill, London (1966))

Fig. 2.12: Lead and Tin in the galvanic series

3. EXPERIMENTAL

3.1 Electroplating

Electroplated Pb-Sn alloy coatings were used to investigate the effect of laser treatment on their corrosion resistance.

Two kinds of electroplated specimens were used:

A: Commercial specimens coated with 15 μ m 40/60 Pb-Sn alloy on 30 μ m electroless copper plated on epoxy resin, and comparing plated and after reflow variants. The reflow process was carried out at the factory by a commercial process, using infra-red radiation.

B: Laboratory-prepared specimens produced by electroplating copper foil with different coating thickness.

3.1.1 Laboratory Electroplatin

A Pb-Sn alloy coating was applied to copper foil, using a commercial tin-lead formula as electrolyte solution in the electroplating bath.

Coating was carried out at room temperature after cleaning and pretreatment of the specimens.

Coating ranging from 2 to about 25 μ m were achieved by varying treatment time between 5 min and 45 min.

The current working density was set at 15 mA/cm² after experiments in the 10 to 20 mA/cm² range.

3.1.1.1 Specimen Preparation and Pretreatment

Substrates for Pb-Sn electroplating had the form of circles, 2.5cm dia. cut out of 0.012 cm copper foil (A.R) (J.T. Baker Chemical Co.). Each specimen was scrubbed with MgO powder and dipped in ethanol (95%) for 5 min in an ultrasonic bath. After this preliminary cleaning it was weighted on an analytical balance. Before electroplating, one side of each of the pair of specimens (see 3.1.1.2 below) was coated with "microstop" lacquer (Tober Division - Michigan Chrome &

Chemical Co.) to prevent electrodeposition. After the lacquer had dried, the specimens were attached to the holder. Immediately before plating, they were dipped for 1 sec. in bichromate acid solution, rinsed off with deionized water, again dipped for 4 sec in 5% fluoroboric acid solution and re-rinsed with deionized water, after were placed in the electroplating set-up.

The weight loss due to copper dissolution, during the pretreatment, was found to be the equivalent of 0.25 μ m thickness.

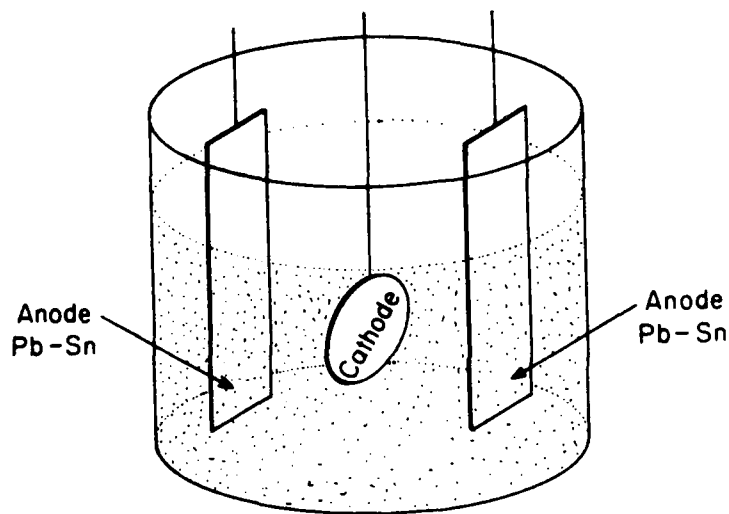


Fig 3.1: Electroplating bath

3.1.1.2 Electroplating Bath

The electroplating bath (Fig. 3.1) consisted of a polyethylene beaker with two Pb-Sn 40/60 anodes on each side of the cathode holder. A pair of substrate specimens were attached to the holder, thereby confining the plating reaction to one side of each specimen.

3.1.1.3 Electroplating Solutions

A. Tin-Lead Alloy Plating Solution

Commercial plating solution for 60/40 tin lead alloy, manufactured by Galvanocor were built up according to the following formula:

Lead fluoborate	41gr/l
Tin fluoborate	120gr/l
Fluoboric acid	140gr/l
Boric acid	10gr/l
Additive L.A.1	15gr/l
Additive L.A.2	15gr/l
Stabilizer L.A.3	10gr/l

The boric acid was dissolved first in 30ml deionized water at 50°C, and other reagents were subsequently added.

B. Fluoboric Aid Solution

Fluoboric acid solution 5% in deionized water was prepared by pouring 5ml of the conc. acid into 95 ml deionized water. About 2gr of boric acid were added in order to prevent HF formation.

C. Bichromate Acid Solution

10gr of potassium bichromate solution were dissolved in 50ml deionized water and 10ml of H₂SO₄ conc. were added. The solution volume was made up to 100ml with deionized water.

3.1.1.4 Electroplating Calculations

A. Current density

Current density was claculated in mA/cm² by dividing the measured current on the cathode by the specimen area.

B. Coating thickness

Coating thickness was calculated according to the equation

$$d_{\mu m} = \frac{g_2 - g_1}{A \cdot \rho} \cdot 10^4$$

where:

- g_1 - specimen weight after electroplating (in grams)
- g_2 - specimen weight before electroplating (in grams)
- A - specimen area (in cm^2)
- ρ - coating density, calculated for 40/60 Pb/Sn alloy (in gr/cm^3)
- d - coating thickness (in μm)

3.2 Laser Operation

The laser used in our experiments was an Nd-YAG model OCR-2A (Quanta-Ray). It was of the pulsed type, working at 532 nm in the visible range with a pulse duration of 7 nsec. The repetition rate was 2 pulses per second. The beam mode was TEM_{10} , in the form of a circle with a hole in the center. The beam diameter outside the apparatus was about 0.5 cm, reduced through an array of focusing lenses to about 100 μm . The radiation impinged perpendicular to the surface (Fig. 3.2). Specimen movements were controlled by a computerized x-y table, whereby the affected zone could be given the form of spots, strips and areas, the latter two being obtained by shifting the specimen during the laser operation so as to produce overlapping between the adjusted pulses.

3.2.1 Laser Energy Calculations

Laser energy per pulse was calculated according to the formula:

$$\text{Joule}/\text{cm}^2 = \frac{W}{R.R.A.J}$$

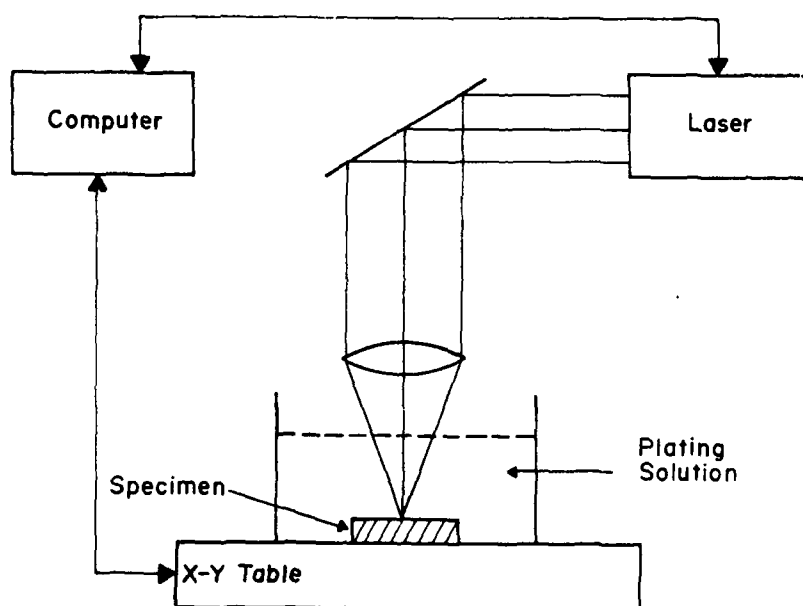
where

- W - energy measured by heat sensitive apparatus (Watt)
- $R.R$ - repetition rate, 2 pulses per second in our experiment
- A - area of laser beam cross section
- J - duration of laser pulse 7 nsec in our experiment

or, in our case,

$$E = \frac{W}{2 \cdot A \cdot 7 \cdot 10^9}$$

Fig. 3.2: Schematic description of experimental set-up



The area of the beam crosssection was calculated from that of the affected zone, but in view of the variability of the latter with the energy, or when more than one pulse was applied, the calculation was based on an average affected area. Example: The average diameter of the affected zone was 100 μ m, and the laser output ranged from $2.5 \cdot 10^{-4}$ watt to $20 \cdot 10^{-4}$ watt. Accordingly, the energy per pulse at $R \cdot R = 2$ ranged from $0.1 \cdot 10^8$ joule/sec to $5 \cdot 10^8$ joule/sec.

3.3 Polarization

Potentiodynamic polarization was carried out in dilute NaCl solution with concentration ranging from 10^{-3} M to 10^{-1} M. The resulting polarization curves provided information regarding the corrosion behavior of the Pb-Sn coating in aqueous solution. Corrosion rates were calculated in milinch per year (MPY) units.

Four types of specimen were polarized:

- (a) Commercial, as deposited.
- (b) Commercial, after reflow.
- (c) Laboratory, as deposited.
- (d) Laboratory, after melting.

3.3.1 Polarization Set-Up

Potentiodynamic polarization curves were obtained with the aid of model 350-A (Princeton Applied Research) set-up.

3.3.1.1 Corrosion Measuring

Data and parameters required for setting up the system before the experiments were entered via the operational push-buttons and stored in the memory. The analysis of each run proceeded automatically according to the setup parameters. Data were collected and stored during the actual run and then played back in the desired format.

The measuring system shown in Fig. 3.3 consisted of (a) a microprocessor control unit; (b) a 365 IR compensation module; (c) a corrosion cell.

The microprocessor control unit included a potentiostat, which varied the potential and measured the current throughout the run according to setup parameters, and an x-y recorder. This unit has the ability of storing the data of the actual run, as well as performing calculations.

The compensation module served for correcting the data on solution resistance.

The corrosion cell system is shown in dismantled form, in Fig. 3.4. The corrosion flask (capacity 2 liters) was fitted with five opening for the various components. The specimen holder, modified by ourselves was mounted in the large central opening and a reference-electrode bridge tube in the angled opening, forming a ball joint; the purge and vent tubes were mounted directly opposite the reference-electrode bridge tube, and the counter-electrode holders in the remaining two openings.

The reference electrode of the saturated calomel type, was inserted in the bridge tube where its bottom contacted the solution in the tube.

The counter-electrodes were made of high-density graphite rod and mounted on each side of the flask. Two leads from the electrometer housing were then connected to the apparatus.

The corrosion cell temperature was controlled by a water bath regulated by contact thermometer to $25^{\circ}\text{C} \pm 2^{\circ}\text{C}$.

Mixing of the solution was effected by a magnetic stirrer and also by the nitrogen gas used in some of the runs (see 3.3.1.2 below) in order to prevent oxygen interference.

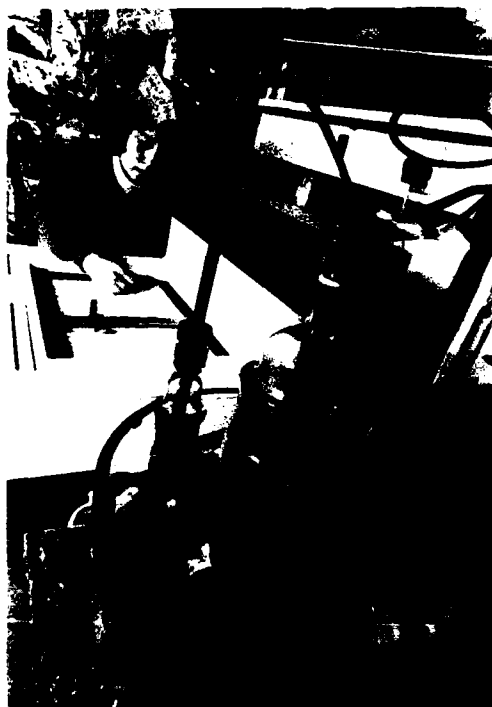


Fig. 3.3: General view of corrosion measuring system.

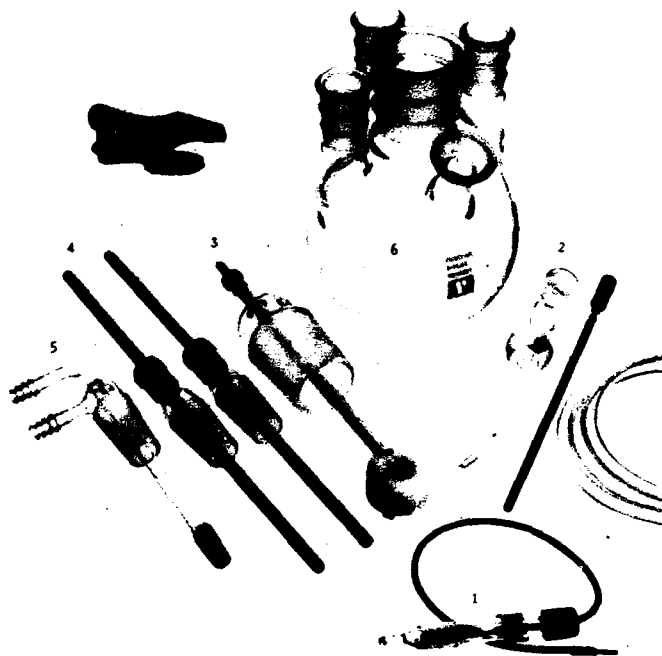


Fig. 3.4: Components of corrosion cell system.

1. Reference electrode (saturated-calomel type)
2. Reference electrode bridge.
3. Specimen holder.
4. Counter-electrodes.
5. Gas purge and vent tubes.
6. Corrosion cell.

3.3.1.2 Experimental Procedure

Preparation of corrosion cell

The corrosion cell was rinsed with deionized water before the electrolyte solution was introduced in an amount sufficient to cover the specimen completely. After the electrolyte, NaCl solution was introduced through the purge tube and bridge tube; the reference and counter electrodes were then mounted and fixed place in the cell.

Thereafter, for nitrogen some of the specimens were bubbled through the solution. After half an hour, the loaded specimen holder was inserted in the solution and the bridge tube position adjusted so that the vycor tip was positioned about 1mm from the surface of the specimen. Continuous mixing was initiated when bubbling began. The system was then left for 5 min in the open potential state, at the $E_{\text{corrosion}}$ level.

Specimen preparation

For electrical contact the outer edges of the coating and the epoxy face of the commercial specimens were painted with colloidal silver, and allowed to dry before the specimen was placed in the holder. (This procedure was not necessary for the laboratory specimen).

Setting up of apparatus

The apparatus was setup during the waiting period required for adjusting the solution. After choosing the technique, the respective parameters were entered.

Some of the specimens were subjected to cyclic potentiodynamic polarization and others to a one way potentiodynamic scan only.

The parameters used for the polarization setup were:

Scan rate: 0.5 mV/sec.

Initial potential (usually) -1.0 volt (versus S.C.E.)

Final potential (usually): 0.0 volt (versus S.C.E.)

Initial delay: 5 minutes.

These parameters were used in all runs with a view to satisfactory comparability.

Run and playback

The runs were initiated by pressing the RUN push-button. First, the initial delay was introduced during which the open circuit potentials were measure. It was followed by the preprogrammed potentiodynamic scan, which began in all runs at a cathodic initial potential; the latter was increased at the desired rate in the anodic direction (with the corresponding current density simultaneously recorded) up to the final level, at which the run ended.

The potential-current readings were plotted by operating the playback mode, the Y-axis representing the voltage and the X-axis the logarithm of the current density. The resulting potentiodynamic polarization curve yielded the relevant Tafel constants, and the corrosion rate was calculated accordingly.

3.4 Modes of Analysis

Optical microscopy was carried out with a Nikon instrument equipped with camera.

Scanning electron microscopy was carried out with a Jeol Model T-200 instrument.

Semi quantitative microanalysis was carried out with an X-ray energy dispersive unit (EDS) model PN200 (Tracor) with the various elements in the coating identified and determined quantitatively by computer.

Surface analyses were carried out by Auger spectroscopy (AES), using a scanning Auger microprobe model 590A (Physical Electronic Ind., Inc.).

X-ray diffraction was carried out in the search for phase transformations induced by the laser treatment

4. RESULTS

4.1 Polarization - Corrosion Resistance Tests

Potentiodynamic polarization was carried out in order to assess the susceptibility of Pb-Sn alloy to corrosion in chloride solution. Corrosion rates of the various specimens and in various chloride concentration were calculated from the polarization curves.

4.1.1 Preliminary Experiments

Preliminary experiments were conducted with commercial specimens that were 15 μ m 40Pb-60Sn deposit on 70 μ m electroless copper coating on epoxy. Half of the samples were after a reflow process. These samples were potentiodynamically polarized at various chloride concentrations ranging from 10^{-3} to 10^{-1} M NaCl. Nitrogen purging was applied in some of the experiments in order to evaluate the dissolved oxygen effects on corrosion resistance.

Figs. 4.1, 4.2 and Table 4.1 summarize these experiments. Typical polarization curves are shown in Fig. 4.1. From these curves we see that the sample underwent general corrosion, both the as-deposited and the reflow specimen. No passivation zone was observed during potentiodynamic polarization of both the as-deposited and the reflow specimen.

For some of the samples, reverse scan was also applied (Fig. 4.1c). The reverse scan was found to be less than the forward scan and no breakdown potential was observed. This behavior shows that the system was a non-localized corrosion system. Table 4.1 and Fig. 4.2 summarize the corrosion rates that were calculated from the potentiodynamic curves. The corrosion rates were calculated in MPY units and ranged from 0.5 to 150 MPY. Table 4.1 and Fig. 4.2 show that for reflow specimen without nitrogen purging the corrosion rate was at maximum at 0.025 MCl⁻ and decreased drastically for higher and for more dilute chloride concentration. The as-deposited specimen with nitrogen purging showed a similar behavior but the decreases in corrosion rates were slight (Fig. 4.2).

It seems from these experiments that nitrogen-purging experiments yielding smaller corrosion rates than the non-purging system, e.g. 40.78 MPY and 0.488 MPY correspond to the corrosion rates observed for the as-deposited specimen during polarization at 0.1 M Cl^- without and with nitrogen purging, respectively. More comparative tests have to be done in order to draw a conclusion.

4.1.2 Polarization of Laboratory Electroplating Samples

Corrosion resistance of various Pb-Sn coating thickness on copper foil were evaluated from potentiodynamic polarization at 10^{-2}M and 10^{-1}M NaCl solutions. In addition to the as-deposited film, specimens after melting at 300°C for 5 sec were also polarized. Figs. 4.3-4.5 show typical polarization curves while Tables 4.2, 4.3 and Fig. 4.6 summarize the results obtained from the potentiodynamic polarization curves.

The typical polarization curves shown in Figs. 4.3, 4.4 and 4.5 were similar and were characterized by an apparent breakdown potential at about -400 mV to -500 mV, that can be due to breakdown of the oxides.

The corrosion potential (E_{corr}) and the corrosion rates (in MPY) were obtained from the potentiodynamic curves. In Table 4.2 results of polarization at 10^{-2}M are given, while in Table 4.3 the results of polarization at 10^{-1}M are summarized. The results of the as-deposited specimens are shown in parts A of the tables while those of the melted ones are shown in parts B of Tables 4.2, 4.3. The tables show a trend of decrease in E_{corr} as the deposit thickness increases. A possible explanation can be the higher effect of the copper base on the E_{corr} of the thinner coating, as a result of a more porous coating. For example, E_{corr} values of -0.726V (S.C.E.) and -0.756V (S.C.E.) were obtained for coating thicknesses of 7.4 μm and 24.3 μm respectively.

The dependence of corrosion rates on coating thickness is shown clearly in Tables 4.2, 4.3 and Fig. 4.6. A decrease in corrosion rate was obtained as the coating thickness increased. For example, corrosion rates of 1.549 MPY and 0.875 MPY were obtained from polarization in 10^{-2}M Cl^- of as-deposited specimens with coating thickness of 7.4 μm

and 23.9 μm respectively. Fig. 4.6a shows this trend very clearly for 10^{-2}M Cl^- solutions, while Fig. 4.6b for 10^{-1}M Cl^- solutions.

The resultant corrosion rates obtained for 10^{-1}M and 10^{-2}M Cl^- ranged from 1.6 MPY to 0.1 MPY. The corrosion rates obtained at 10^{-2}M Cl^- solution ranged from 1 MPY to higher values while for 10^{-1}M Cl^- solution from 1 MPY to lower values (Fig. 4.6).

Comparison between the as-deposited and melted specimens shows that the melted surfaces have smaller corrosion rates than the as-deposited ones. For example, 1.427 MPY against 0.976 MPY for as-deposited and melted specimens respectively (Table 4.2). No clear trend was observed as to the effect of the solidification process on E_{corr} values.

For technical reasons and lack of time, corrosion test of laser-treated surface were not done and will be carried out during the second year of the project.

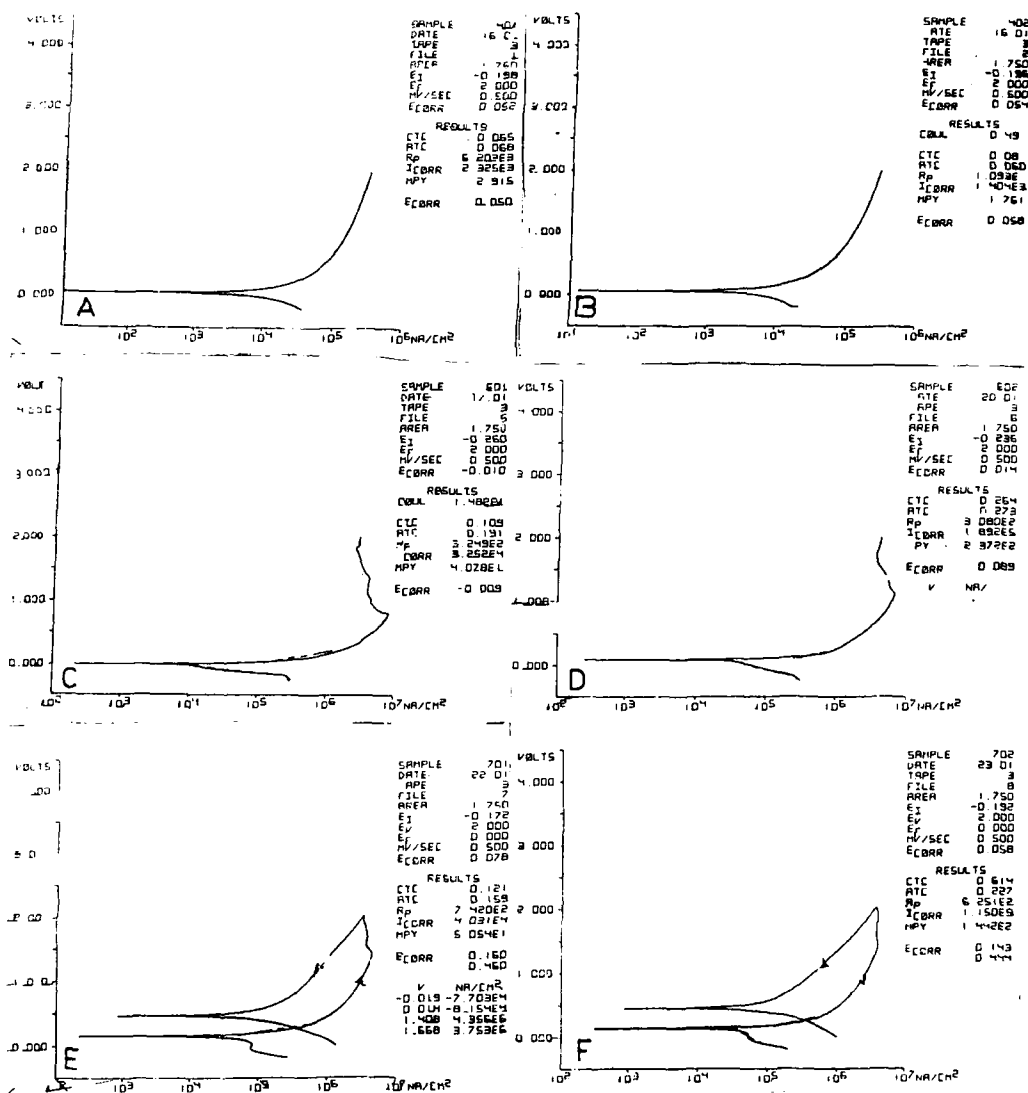


Fig. 4.1

Typical potentiodynamic curves obtained for Pb/Sn commercial specimen. A. As deposited specimen polarized at $10^{-3}M$ NaCl. B. Specimen after reflow polarized at $10^{-3}M$ NaCl. C. As-deposited specimen polarized at $10^{-3}M$ NaCl. D. Specimen after reflow polarized at $10^{-3}M$ NaCl. E. As-deposited specimen polarized at $2.5 \cdot 10^{-2}M$ NaCl. F. Specimen after reflow polarized at $2.5 \cdot 10^{-2}M$ NaCl.

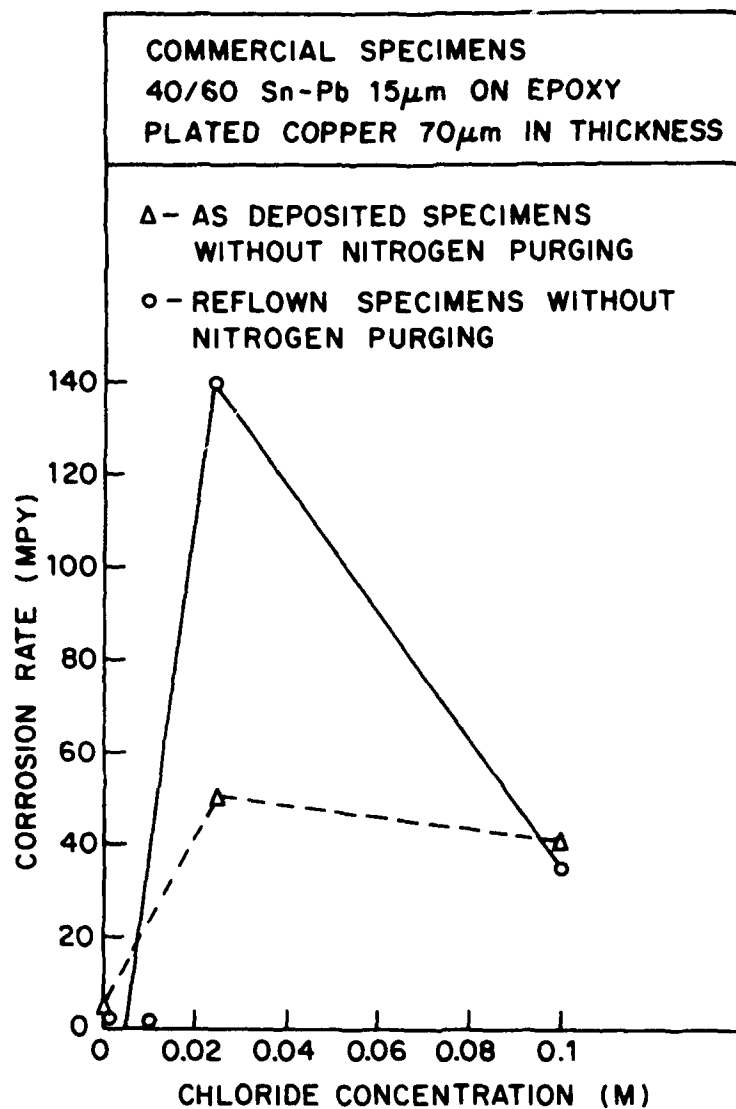


Fig. 4.2: Effect of chloride concentration on Pb-Sn corrosion rate.

Table 4.1 Results of Preliminary Potentiodynamic Polarization of Commercial Specimen

Table 4.1 Results of preliminary potentiodynamic polarization of commercial specimen

No.	Reflow +/-	N ₂ Purge +/-	NaCl Mol/l	MPY
101	-	+	0.025	
102	+	+	0.025	
301	-	+	0.025	
302	+	+	0.025	
401	-	-	0.001	2.915
402	+	-	0.001	1.761
501	-	-	0.01	-
502	+	-	0.01	1.545
601	-	-	0.1	40.78
602	+	-	0.1	35.53
701	+	-	0.025	50.54
702	+	-	0.025	144.2
801	+	-	0.1	0.488
802	+	+	0.1	0.954

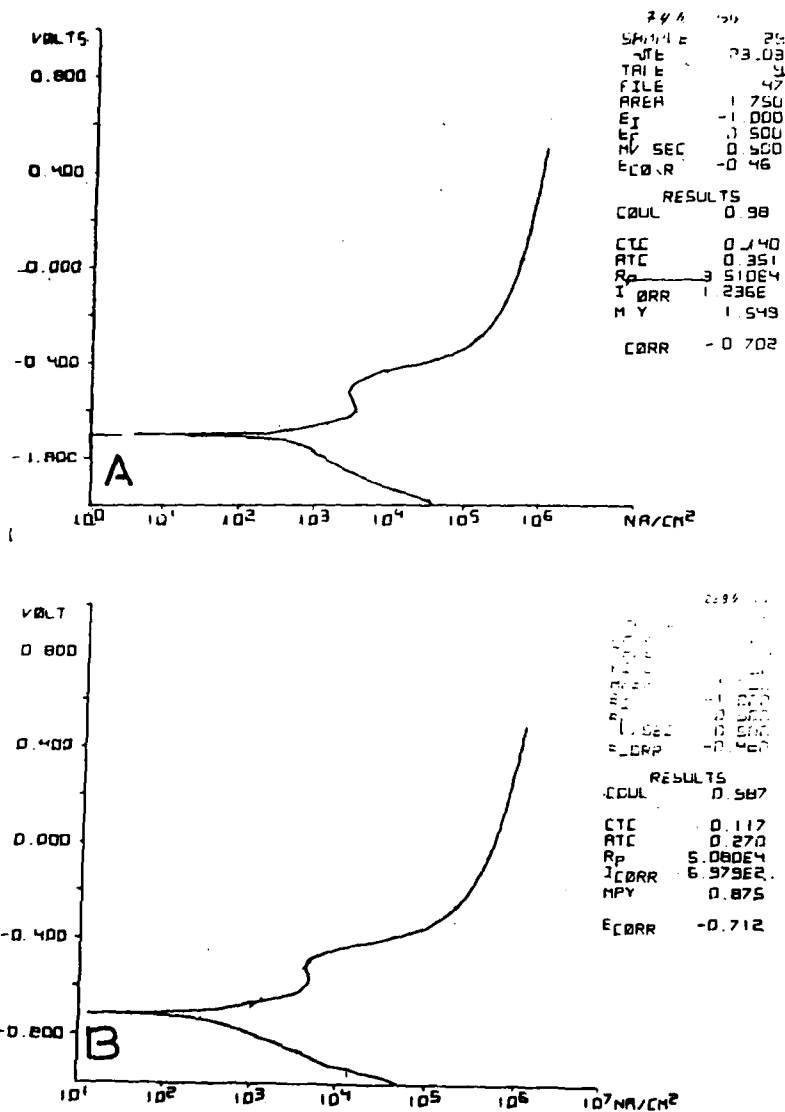


Fig. 4.3: Typical curves obtained during potential-dynamic polarization of Pb-Sn specimen with various coating thickness at 10^{-2}M NaCl.
 A. Coating thickness 7.4 μm .
 B. Coating thickness 23.9 μm .

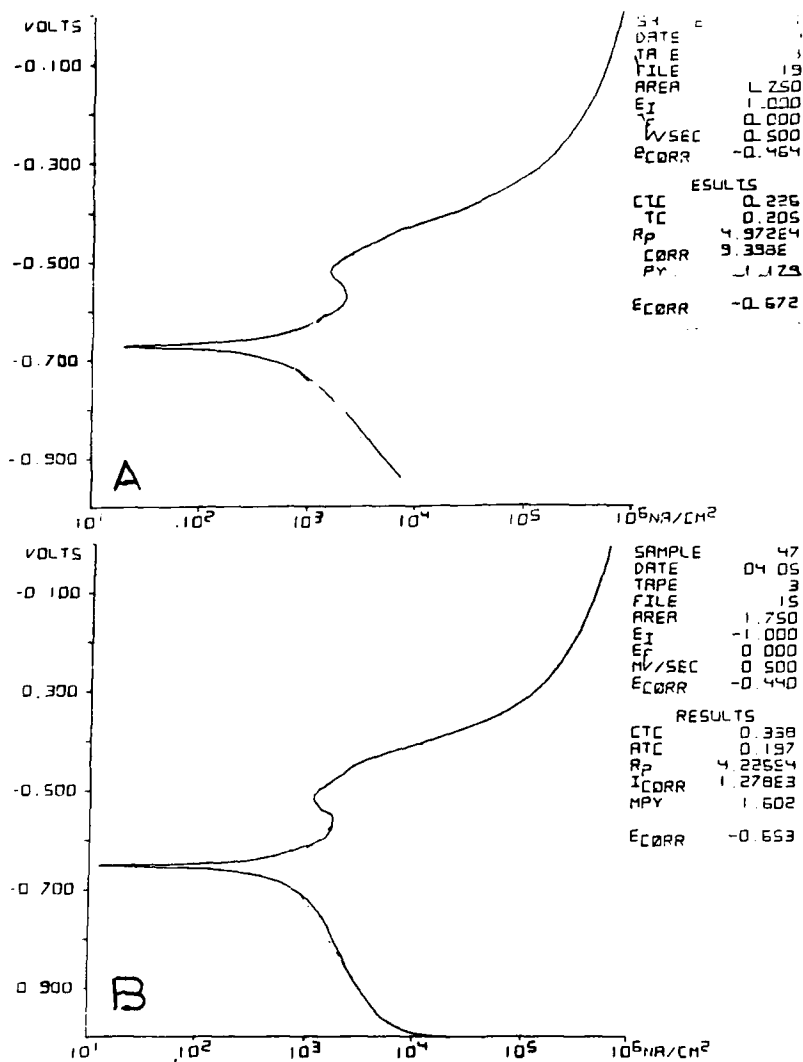


Fig. 4.4: Typical curves obtained during potentiodynamic polarization of Pb-Sn specimen after melting with various coating thickness at $10^{-2}M Cl^{-}$.
 A. Coating thickness $2.7\mu m$.
 B. Coating thickness $24.2\mu m$.

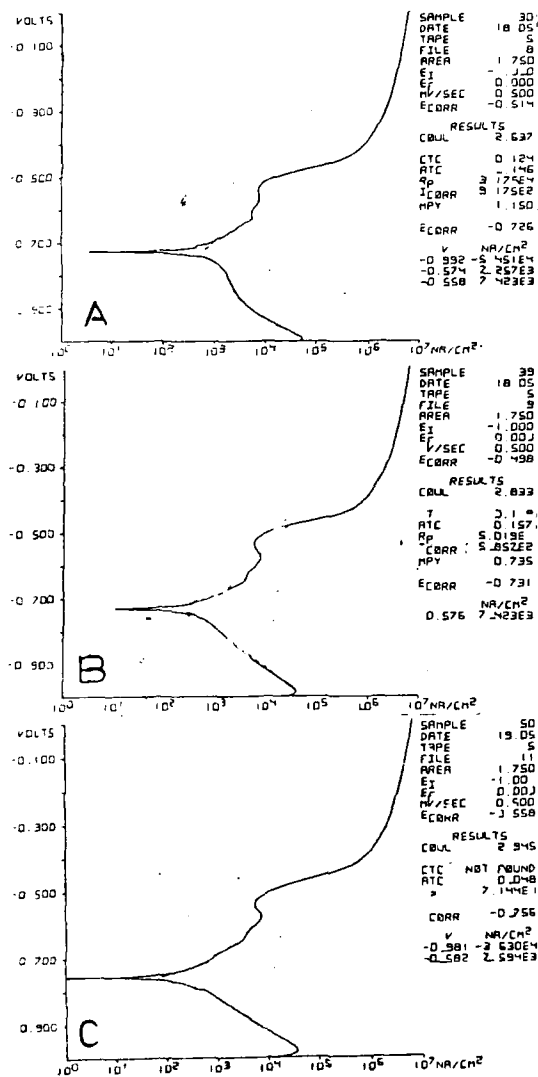


Fig. 4.5: Typical curves obtained during potentiodynamic polarization of Pb-Sn coating at 10^{-1}MCl^- .

- A. Coating thickness 7.4 μm .
- B. Coating thickness 11.8 μm .
- C. Coating thickness 24.3 μm .

Table 4.2a Summary of potentiodynamic polarization corrosion tests at 10^{-2} M NaCl with nitrogen purging - as-deposited

Specimen No.	22	23	38	46	52
Coating Thickness Mm	2.8	7.4	11.7	18.1	23.9
MPY	-	1.549	1.427	1.084	0.615
E_{corr} V(S.C.E.)	-0.581	-0.702	-0.716	-0.720	-0.711

Table 4.2b Corrosion test at 10^{-2} M NaCl with nitrogen purging after melting in oven at 300°C

Specimen No.	21	27	35	41	47
Coating thickness Mm	2.7	5.5	9.7	16.5	24.2
MPY	1.179	0.801	0.976		1.602
E_{corr} V(S.C.E.)	-0.672	-0.732	-0.645		-0.657

Table 4.3a: Corrosion test results at 10^{-1} M NaCl with nitrogen purging - as-Deposited

Specimen No.	30	39	45	50
Coating thickness μm	7.4	11.8	18.3	24.3
MPY	1.150	0.735	0.191	-
E_{corr} v (S.C.E.)	-0.726	-0.731	-0.76	-0.756

Table 4.3b Corrosion tests at 10^{-1} M NaCl with nitrogen purging - after melting in oven at 300°C

Specimen No.	28	40	44	51
Coating thickness μm	5.5	11.5	17.3	23.9
MPY	0.320	0.298	0.465	0
E_{corr} V(S.C.E.)	-0.734	-0.688	-0.769	-0.771

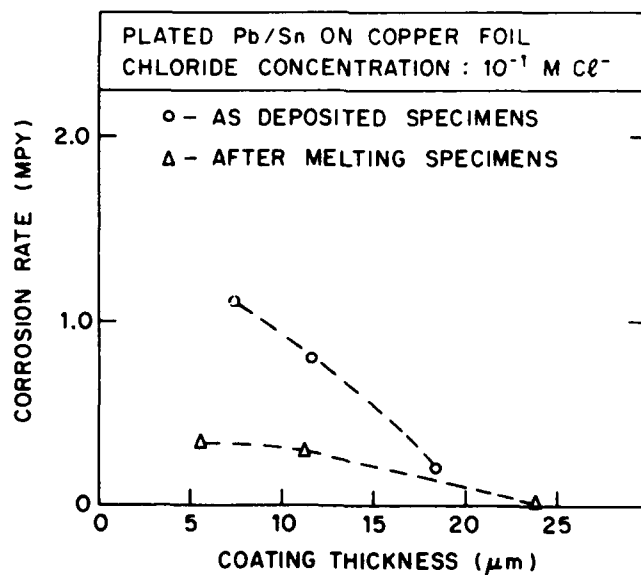
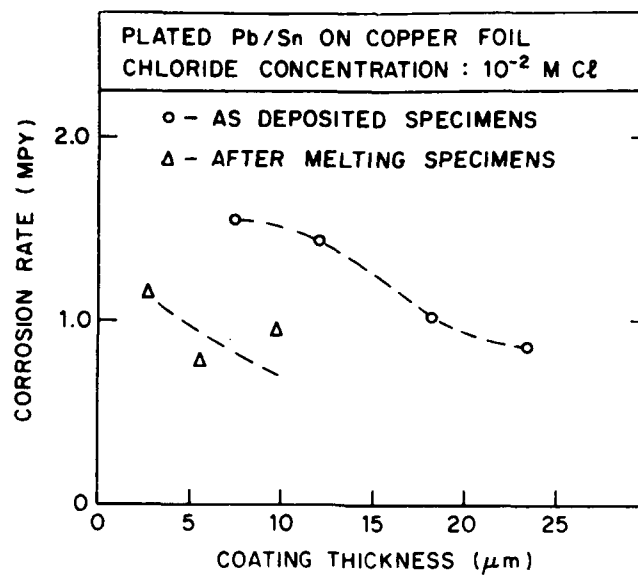


Fig. 4.6: Corrosion rates of Pb-Sn coating vs. coating thickness. A. In 10^{-2} M Cl^- . B. In 10^{-1} M Cl^-

4.2 SEM Observations After Polarization

Figs. 4.7 to 4.15 are SEM observations of the surface of the specimens corroded as described in Chapter 4.1. Figs. 4.7 to 4.10 are SEM observations of commercial specimens after polarization, while Figs. 4.11 to 4.15 show the corroded surface areas of the laboratory prepared specimens.

4.2.1 Commercial Specimens

SEM observations of commercial specimen areas before and after corrosion, shown in Figs. 4.7 to 4.10, revealed the following phenomena. The morphology of the as-deposited coating surface before polarization differed from that of the reflow specimen. For example, we see in Fig. 4.7A the surface of as deposited commercial specimens and in Fig. 4.7B the surface of reflow specimen. The morphology of the area shown in Fig. 4.7A was porous but separate zones were not observed; by comparison, the surface shown in Fig. 4.7B for the reflow specimen was smooth but contained brighter zones with a very high concentration of Pb, as shown clearly in Fig. 4.8.

Fig. 4.8A shows the E.D.S. semiquantitative analysis of the uncorroded area of the as-deposited specimen: 43.6% Pb; 54.3% Sn; 1% Cu. The reflow area composition analysis were as follows. The composition of the bright areas shown in Fig. 4.7 was 88% Pb, 10% Sn, while the composition between the bright zones was: 32%Pb, 67% Sn. The overall composition was 40% Pb and 58% Sn.

Figs 4.9, 4.10 show the corroded areas of the commercial specimen. In Fig. 4.9A, 4.9B, the Pb-Sn coating was dissolved almost totally, as can be seen by the composition which was mostly copper (66.1%) for the as-deposited specimen and contained only 4.9% Pb for the reflow specimen (Fig. 4.9B). Crystals rich in copper were found, possibly copper chloride crystals. From Figs. 4.9, 4.10 we see also that Pb dissolved more rapidly than Sn. For example, 5.1% Pb and 58.0% Sn remained after polarization in the corroded area shown in Fig. 4.10A.

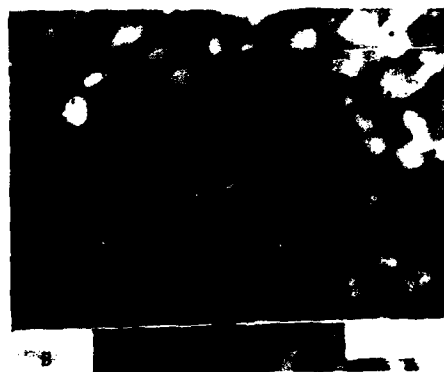
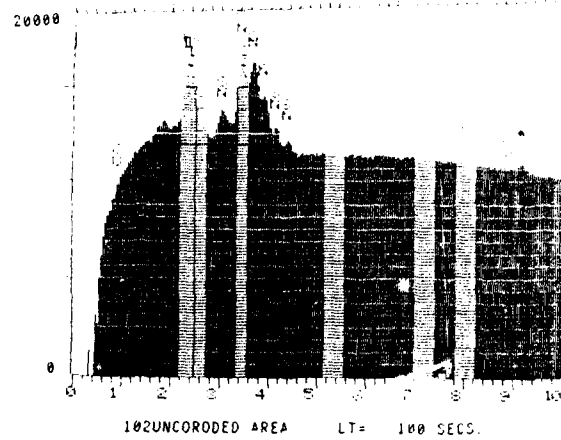
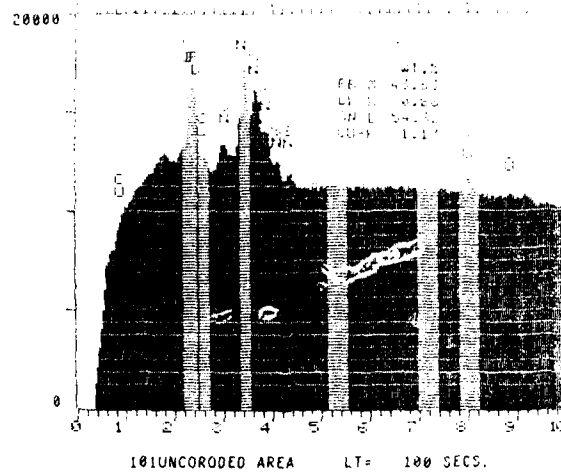
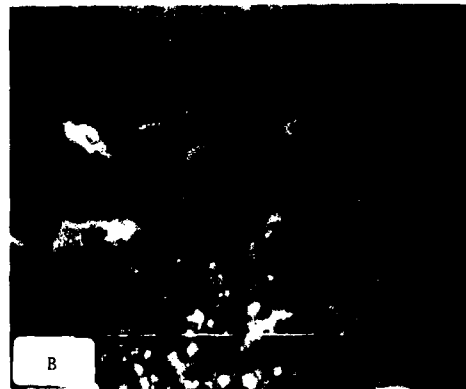
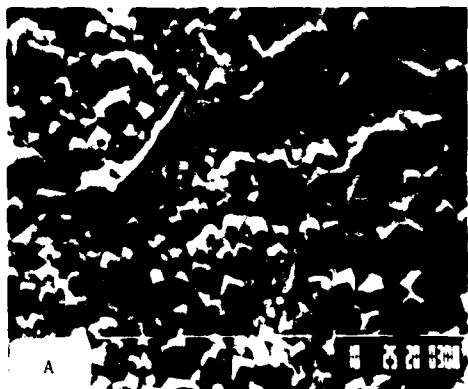


Fig. 4.7: Surface SEM observations of commercial Pb-Sn 40/60 deposits on epoxy plated 70 μ m copper.
A. As-deposited x5000. B. After reflow x5000.



WT %		Area	Bright Zone	Between Bright Zone
	Pb	40	88	32
	Sn	59	10	67
	Cu	1	1	0.5

Fig. 4.8: E.D.S. results of area shown in Fig. 4.7.
A. As-deposited area.
B. Reflow area.



Area Composition

	wt%
Cu	66.1
Pb	1.8
Cl	17.1
Sn	15.0

Crystal Composition

	wt%
Cu	79.3
Pb	1.6
Cl	11.8
Sn	7.3

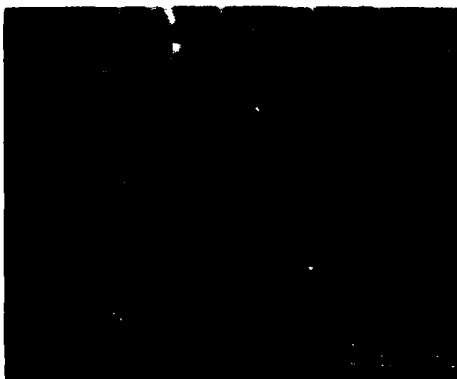
Area Composition

	wt%
Cu	28.8
Pb	4.9
Cl	14.0
Sn	53.0

Crystal Composition

	wt%
Cu	57.7
Pb	3.9
Cl	19.6
Sn	18.7

Fig. 4.9: Surface SEM observations of 40/60 Cu-15/15 Sn-40/60 deposited on epoxy plated 100μm copper. Deposited were polarized at 0.025M Cl⁻ without purging nitrogen.
A. As-deposited specimens.
B. Specimen after reflow. (See Fig. 4.2).



Area Composition

	wt%
Cu	24.0
Pb	5.1
Cl	12.8
Sn	58.0

Area Composition

	wt%
Cu	44.7
Pb	3.8
Cl	24.7
Sn	27.0

Fig. 4.10: Surface SEM observations of commercial Pb-Sn 40/60 deposited on epoxy plated 70µm copper. Deposited were polarized at 0.1M Cl⁻ without purging nitrogen.

A. As-deposited specimens.

B. Specimen after reflow.

4.2.2 Laboratory Specimens

Figs. 4.11 to 4.15 show SEM observations of the corroded area morphology after potentiodynamic polarization of laboratory prepared specimens with various coating thickness. Fig. 4.11 shows corroded areas of as-deposited specimen after polarization in $10^{-2}M$ NaCl, Fig. 4.12 the same area at higher magnification, and Fig. 4.13 the E.D.S. analysis of these areas. Figs. 4.11A, 4.12A and 4.13A show that the corroded area of $2.8\mu m$ Pb-Sn coating was mostly copper chloride as can be seen clearly from the elements composition of the area: 19.7% Cl; 1.3% Pb, 23.5% Sn and 55.5% Cu (Fig. 4.13A). Specimens with thicker coatings ($7.4\mu m$ and $11.7\mu m$) exhibited a corroded area with a highly ordered structure (Figs. 4.11B,C, 4.12B, C) in which the E.D.S. analysis revealed the presence of only Sn, e.g., 0.8% Cl, 6.9% Pb, 92.3% Sn and 0% Cu (Fig. 4.13C). Comparison between these corroded areas and the uncorroded areas (Figs. 4.12D, 4.13D) suggested dissolution of Pb only during polarization process which led to an Sn ordered structure.

The heat treated specimens ($300^{\circ}C$ in oven for 4 sec.) before and after polarization exhibited a slightly different behavior. The corroded areas show hole formation in the coating surface compared with the uncorroded areas (Figs. 4.14, 4.15). The E.D.S. element analysis summarized in Table 4.4 provided information on Pb dissolution during polarization hence an increase in Sn content. For example, for coating thickness of $16.5\mu m$ 39% Pb and 60% Sn were detected before polarization as against 24% Pb and 75% Sn after polarization. Fig. 4.16 show that Pb dissolution was more or less at a constant ratio to the initial Pb content; between 30% to 40% of the initial Pb content were dissolved.

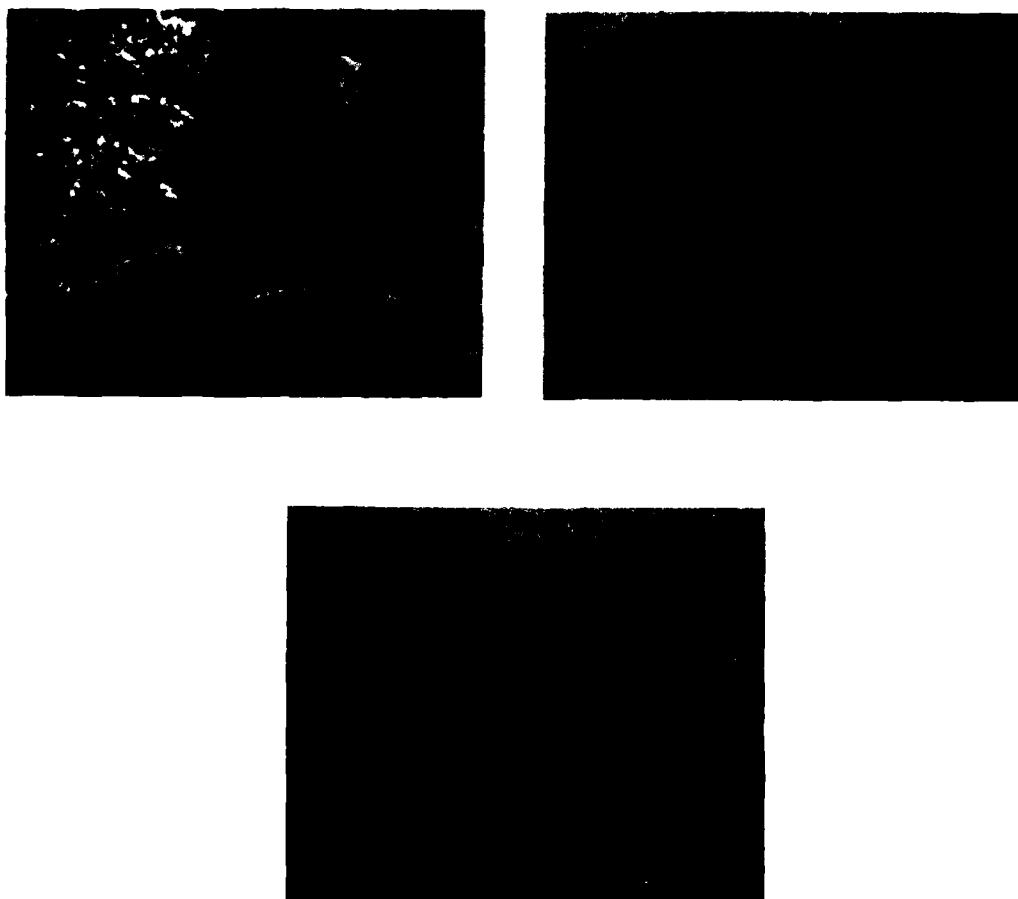


Fig. 4.11: SEM observations of corroded areas after potentiodynamic polarization at 10^{-2}M NaCl of specimen with various Pb-Sn coating thickness. A. Coating thickness $2.8\mu\text{m}$ x1500. B. Coating thickness $7.4\mu\text{m}$ x1500. C. Coating thickness $11.7\mu\text{m}$ x1000. (No. 22, 29, 38).

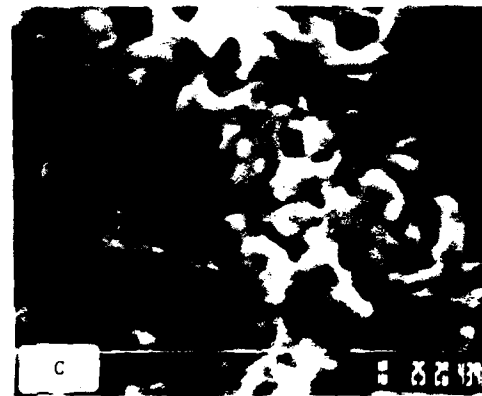
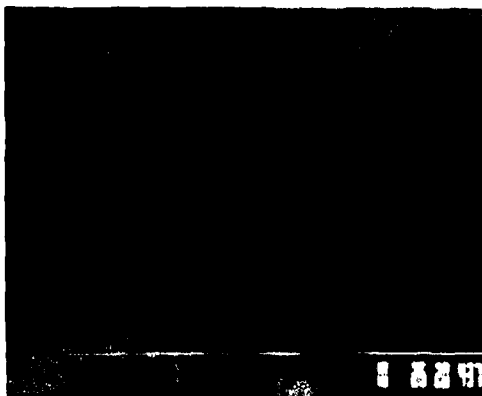


Fig. 4.12: SEM observations of corroded and uncorroded surfaces of specimen with various Pb-Sn coating thickness after polarization in 10^{-2} M NaCl.

- A. Coating thickness $2.8\mu\text{m}$ x7500.
- B. Coating thickness $7.4\mu\text{m}$ x7500.
- C. Coating thickness $11.7\mu\text{m}$ x7500
- D. Uncorroded area, $7.4\mu\text{m}$ x7500.

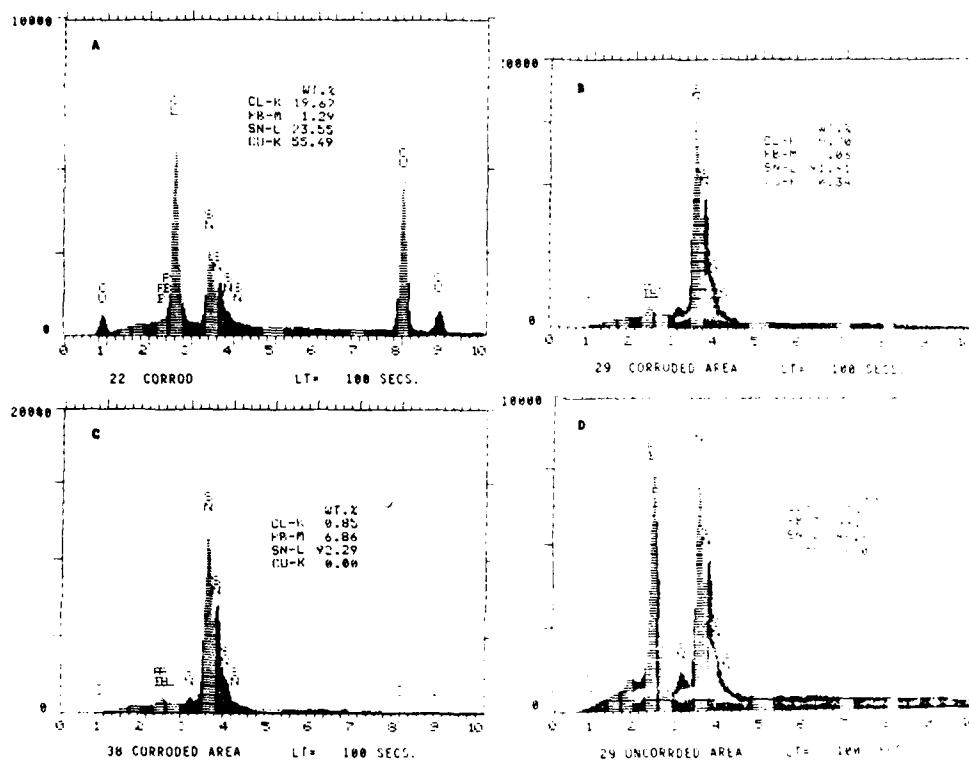


Fig. 4.13: EDS microanalysis of corroded and uncorroded specimen of various thickness. Polarization in $10^{-2}M$ Cl.

- A. 2.8 μm .
- B. 7.4 μm
- C. 11.7 μm
- D. Uncorroded 7.4 μm

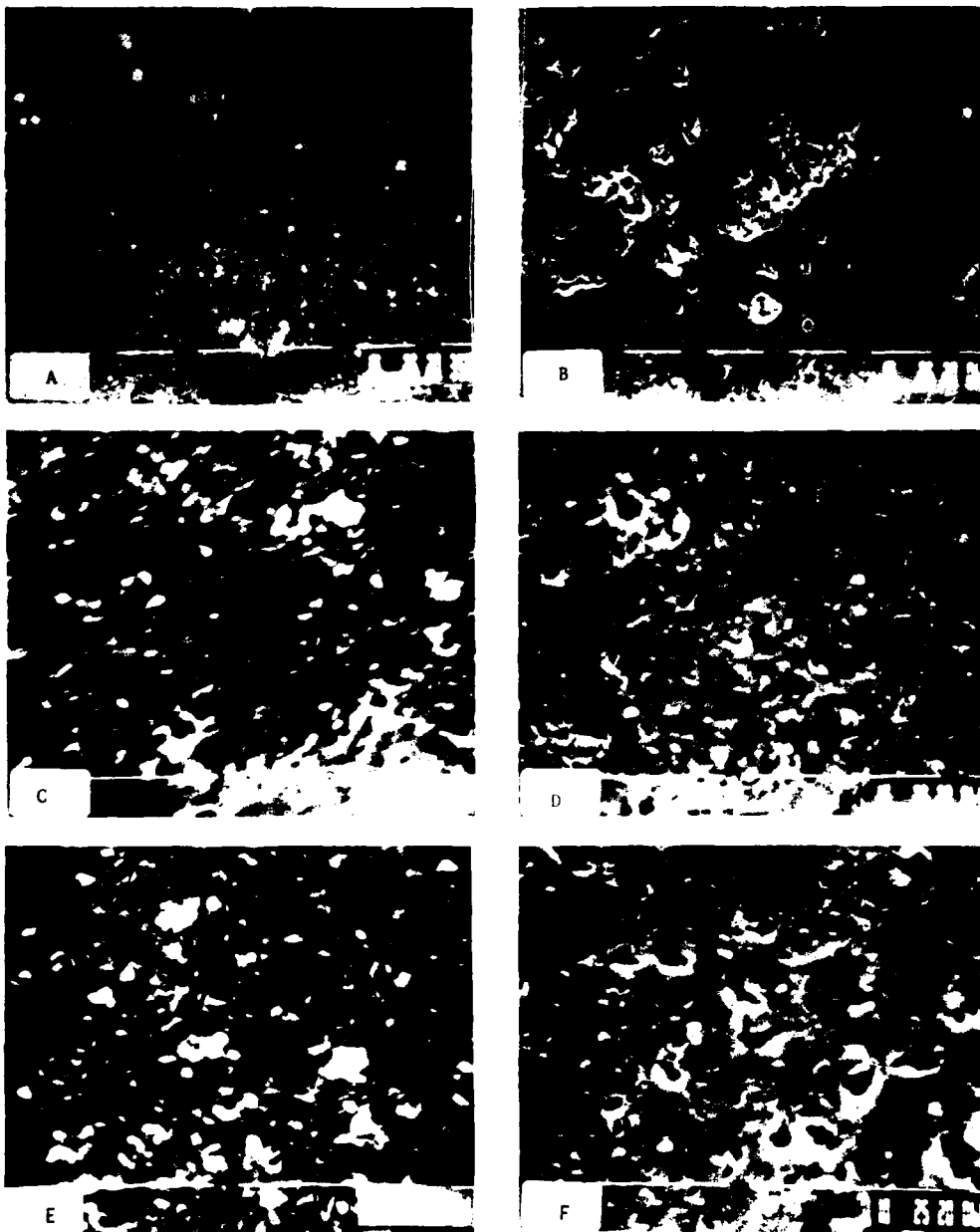


Fig. 4.14: SEM observations of heat treated specimen before and after potentiodynamic polarization - 10⁻²M NaCl at various thicknesses.
 A. 2.7 μm before polarization, x1500.
 B. 2.7 μm after polarization, x1500.
 C. 5.5 μm before polarization, x5000.
 D. 5.5 μm after polarization, x5000.
 E. 9.7 μm after polarization, x5000.
 (No. 21, 27, 35).

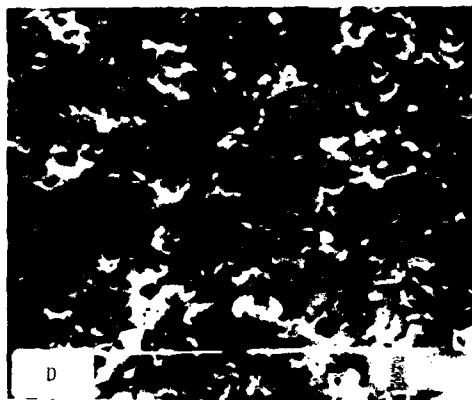
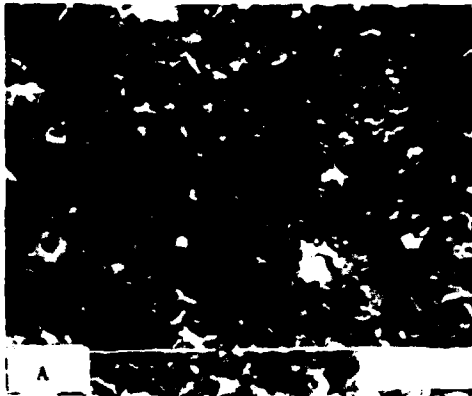


Fig. 4.15: SEM observations of heat treated specimen before and after potentiodynamic polarization in 10^{-2}M NaCl at various thickness.

- A. 16.5 μm before polarization, x5000.
- B. 16.5 μm after polarization, x5000.
- C. 24.2 μm before polarization, x5000.
- D. 24.2 μm after polarization, x5000.

Table 4.4: Summary of E.D.S. analysis of laboratory specimen before and after polarization

Table 4.4 Summary of E.D.S. analysis of laboratory specimen before and after polarization

Sample No.	Thickness μm	Melting +/-	Corrosion process +/-	Area Composition - Wt %			
				Pb	Sn	Cu	Cl
21	2.7	+	-	51.85	50.46	6.19	
	2.7	+	+	50.99	54.25	6.20	0.47
27	5.5	+	-	54.46	50.17	1.45	
	5.5	+	+	22.64	70.47	1.46	0.47
35	9.7	+	-	40.21	56.77	0.47	
	9.7	+	+	26.78	68.38	4.1	0.42
41	16.5	+	-	39.19	60.45	0.36	
	16.5	+	+	21.15	71.83	0.61	0.37
42	24.2			42.09	57.37	0.54	
	24.2			29.52	69.7	0.50	0.47
22	2.8	-	+	1.29	23.55	55.49	19.67
29	7.4	-	-	49.79	48.87	0.01	
7.4	+	+	7.06	91.91	0.34	0.70	
38	11.7	-	+	6.66	92.29	0	0.05

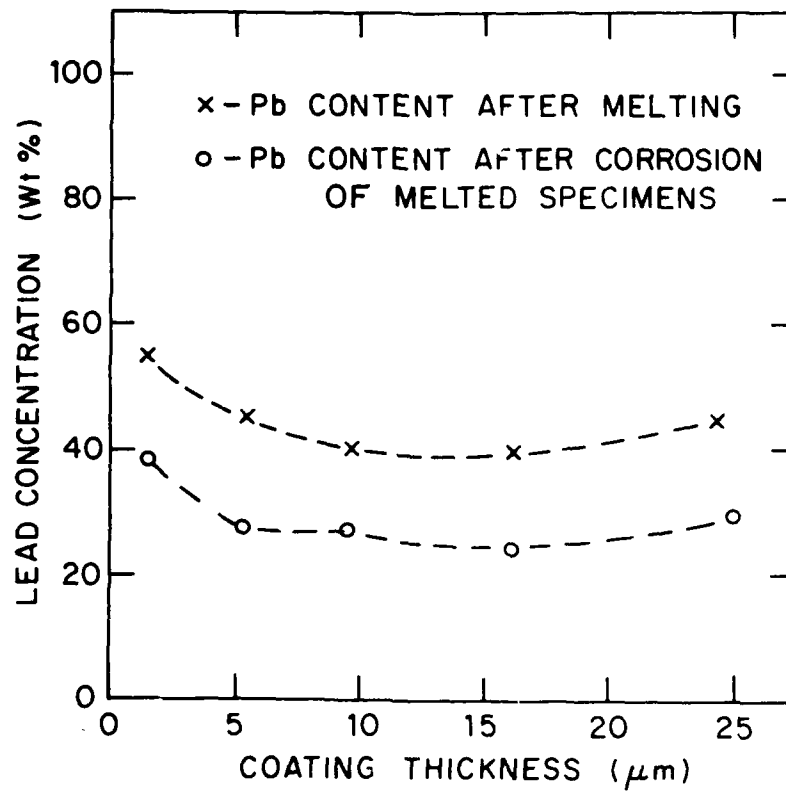


Fig. 4.16: Effect of polarization on lead concentration for various coating thicknesses

4.3 Laser Treatment

4.3.1 Laser Experiments - Lines

Nd-YAG pulse laser at 530 nm was used to treat the Pb-Sn alloy coating in order to produce heat treated zones in a mode that can be a substitute to the reflow process for small limited areas. It is also believed that better corrosion resistance will be achieved at the laser treated surfaces. The first stage of the experiment was to define the laser working conditions and its effects on the treated surfaces. Initial experiments were done on Pb-Sn coating (6.8 μm thickness) when lines were produced as can be seen in Fig. 4.17 for three laser intensities. Figs. 17a,b were for the lowest and Fig. 17e,f for the highest laser energy. Melting zones treated with laser are seen in Fig. 17 b,d,f. The shape of the laser pulse cross-section is seen clearly in Fig. 17a but as the energy increases the melted zone adopted a more complex form (Figs. 17c,e). The melted zones differed from the untreated areas as can be seen clearly from Figs. 4.18. The as-deposited area (Fig. 4.18a) shows a packed pile in which separate single grains are visible. The laser-treated area revealed the footprint of the laser pulses at lower magnification, (Figs 4.17a,c,e) and a change in area morphology at higher magnification (Fig. 4.18b). The melted area exhibited smoother morphology at higher magnification in comparison to the as-deposited specimen brighter areas, Pb-rich zones were observed at the laser located areas.

Figs. 4.19 are SEM observations of laser treatment of 2.7 μm thickness Pb-Sn coating with various laser intensities ranged from $2 \cdot 10^8$ watt/cm² (Fig. 4.19a,b) to $6 \cdot 10^8$ watt/cm² (Fig. 4.19e,f). The melted zone higher magnification observations are shown in Fig. 4.20. The main features observed in Fig. 4.19 were the complex form produced by laser treatment and the formation of a halo that surrounded the lines. As the laser intensity was increased the line form became more complex and a wider halo was produced. The difference between the treated zones and the as-deposited materials is shown clearly in Figs. 4.20a,c,e where the line edges are seen in details. The high magnification Figs. 4.20 b,d,f show the details of the melted area.

From Figs. 4.20 it is seen that for the lowest laser intensity (Fig. 4.20 a) the melted zone was above the background while for the highest energy (Fig. 4.20c) the

melted zone level is beneath the untreated area. This observation is confirmed by the E.D.S. results shown in Table 4.5: increase in copper content as the laser energy was increased, which meant a deeper effect of the laser treatment.

For better understanding of the laser interference with the Pb-Sn coating, we applied laser treatment under various conditions without moving the specimens.

Table 4.5 E.D.S. microanalysis of laser treated zone with various laser intensities

	Pb Wt%	Sn Wt%	Cu Wt%
Background without laser	54.1	44.7	1.2
Laser pulse intensity $2 \cdot 10^{-8}$ watt/cm ²	54.2	43.8	2.0
Laser pulse intensity $4 \cdot 10^{-8}$ watt/cm ²	51.9	45.8	2.3
Laser pulse intensity $6 \cdot 10^{-8}$ watt/cm ²	52.0	44.2	3.7

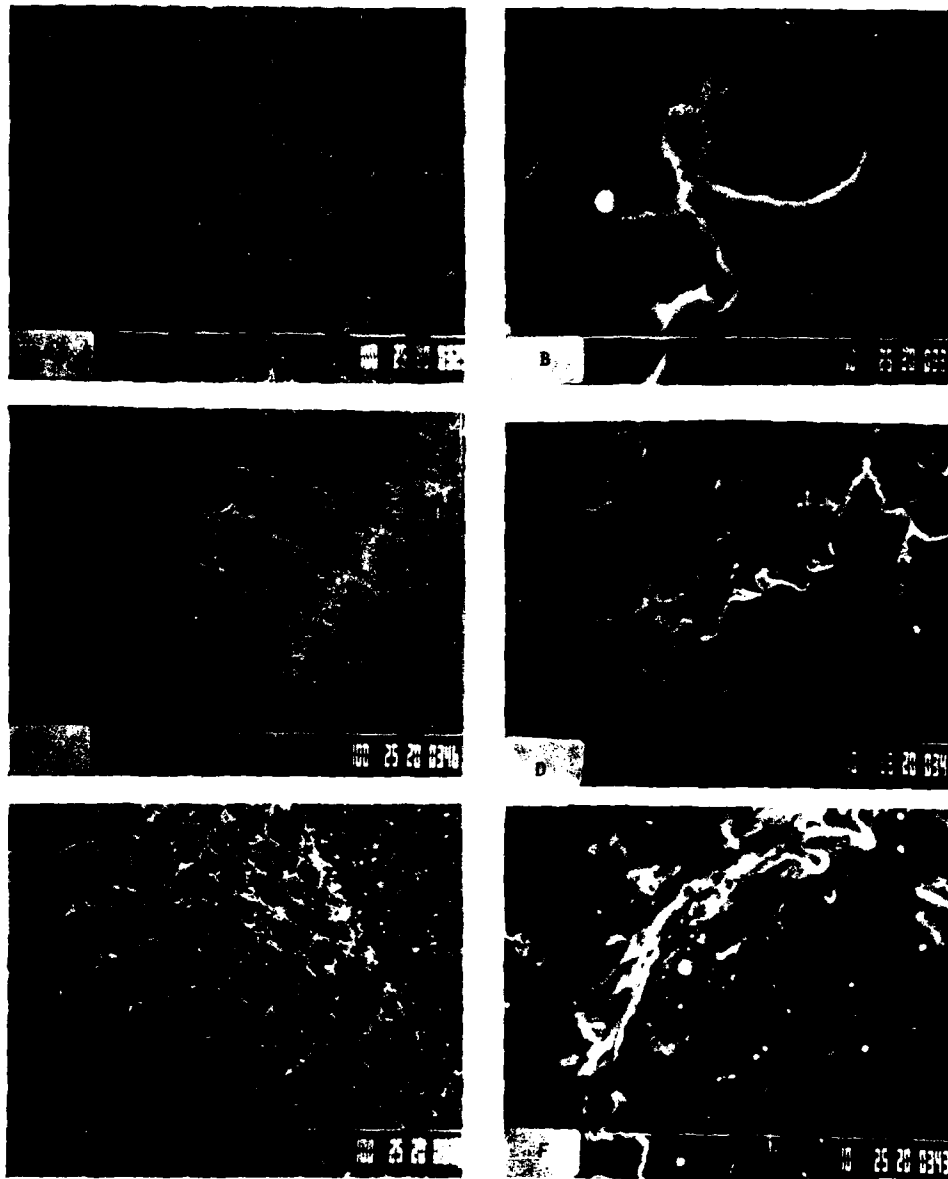
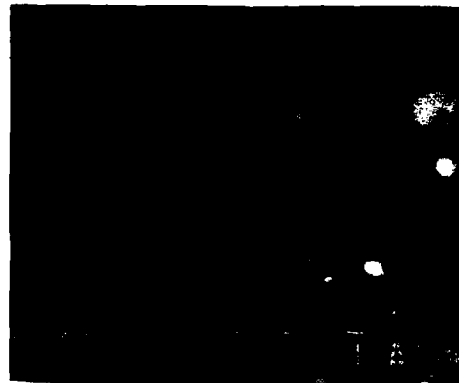
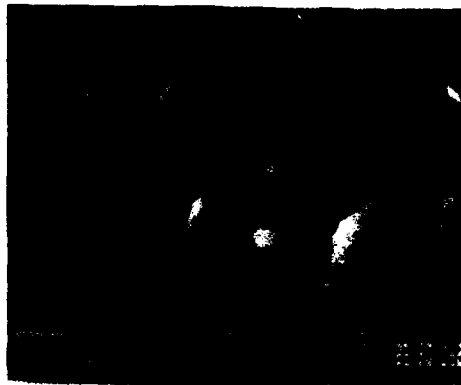


Fig. 4.17 SEM observations of laser treated surfaces at various laser pulse power densities (Rep. rate 2Hz, overlap 0.5 scan speed 50 $\mu\text{m}/\text{sec}$). Pb-Sn coating thickness 6.8 μm .

- A. $1.0 \cdot 10^7$ watt/ cm^2 (x150).
- B. Enlargement of line shown in A x5000.
- C. $1.0 \cdot 10^8$ watt/ cm^2 , x150.
- D. Enlargement of line shown in C, x1500.
- E. $2.5 \cdot 10^8$ watt/ cm^2 , x150.
- F. Enlargement of line shown in E, x1500.



Background Composition

	Wt%
Pb	47.2%
Sn	51.8
Cu	1.0

Line Composition

	Wt%
Pb	39.00
Sn	60.0
Cu	1.0

Fig. 4.18: SEM observations of 6.8μm Pb-Sn coating on copper foil.
 A. Without laser treatment, x10,000.
 B. After laser treatment at pulse power density 1.107. x10,000.

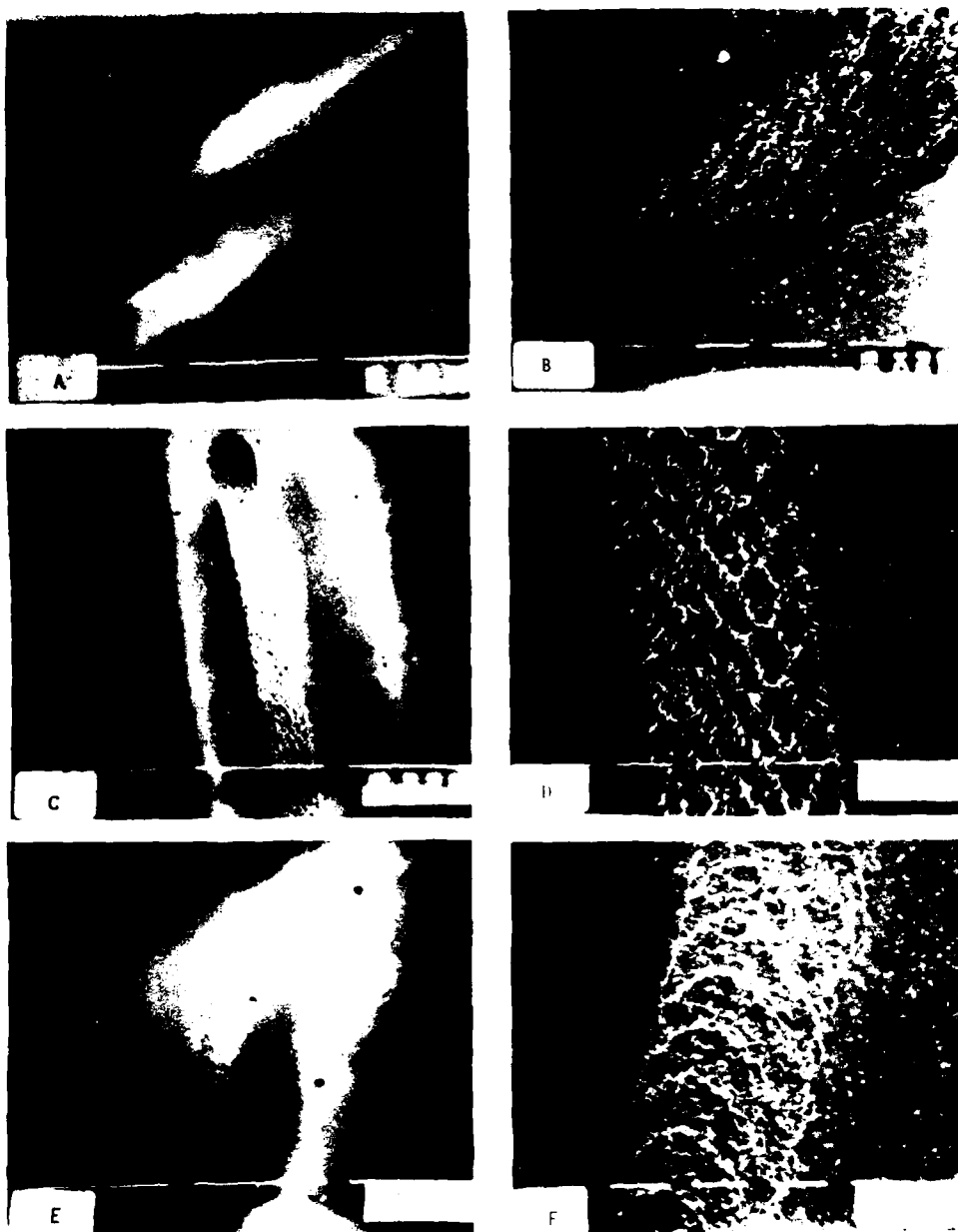


Fig. 4.19: SEM observations of lines formed by laser treatment on 2.7 μ m Pb-Sn coating, with various pulse power densities. (Rep. rate 2Hz, overlap 0.5 scan speed 50 μ m/sec.).

- A. 2.10⁸ watt/cm², x3.5.
- B. Enlargement of A x150.
- C. 4.10⁸ watt/cm², x35.
- D. Enlargement of C, x150.
- E. 6.10⁸ watt/cm², x35.
- F. Enlargement of E, x150.

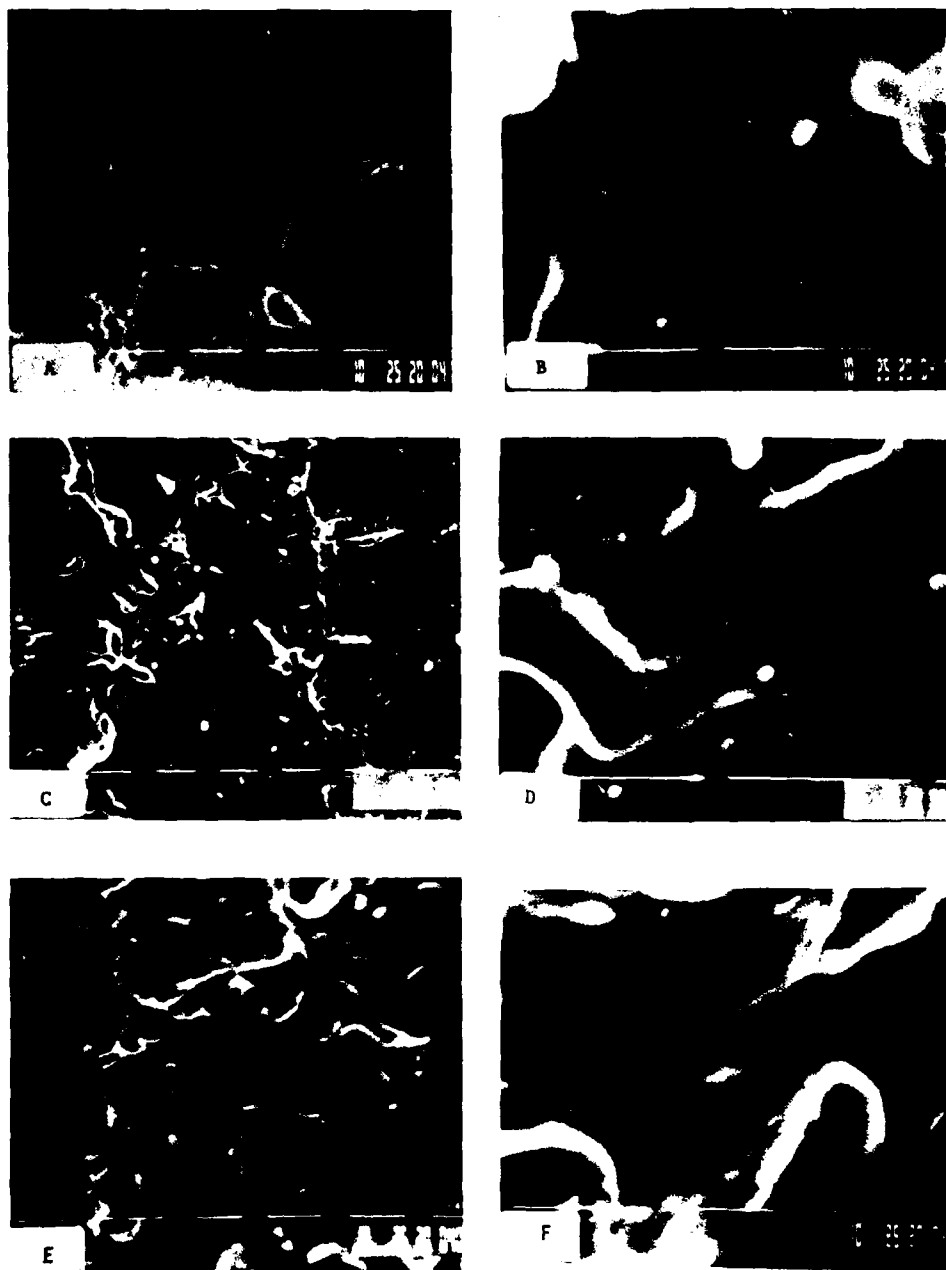


Fig. 4.20: Enlargement of area shown in Fig. 4.19.
 A. $2 \cdot 10^8$ watt/cm² line side, x1500.
 B. $2 \cdot 10^8$ watt/cm² line center, x5000.
 C. $4 \cdot 10^8$ watt/cm² line side, x1000.
 D. $4 \cdot 10^8$ watt/cm² line center, x5000.
 E. $6 \cdot 10^8$ watt/cm² line side, x1500.
 F. $6 \cdot 10^8$ watt/cm² line center, x5000.

4.3.2 Laser Experiments - Spots

Figs. 4.21 to 4.26 are SEM spot observations taken under different conditions. Laser intensity and pulse number were varied and spots were formed on the Pb-Sn coating reflecting the difference in laser treatment conditions. For each laser intensity the pulse numbers per spot were 1, 2, 3, 5 and 10 pulses.

In Fig. 4.21 the single pulse variant is shown with pulse energy density ranging from $0.25 \cdot 10^9$ watt/cm² to $1.8 \cdot 10^9$. The smallest affected area was observed for the lowest energy used, while for the higher energy densities (Figs. 4.21a,b) the laser produced depth effects in the form of a circular crater.

Fig. 4.22 shows the influence of pulse number for the highest energy density used in this experiment. The shallowest effect was observed for the area produced by a single pulse (Fig. 4.21) and two pulses (Fig. 4.22), and crater depth increased with the number of pulses. For five and ten pulses layers were formed at the edge of the craters, their number also increasing with the number of pulses. The center of each crater was depressed relative to its edges.

The same phenomenon is seen in Figs. 4.23, 4.24 and 4.25 for energy densities $1.44 \cdot 10^9$, $0.55 \cdot 10^9$ and $0.25 \cdot 10^9$ watt/cm², respectively. It is clear that as laser intensity decreases, so do the radius and depth of the affected area.

Fig. 4.27 summarizes the information of the above experiments. The diameter of the affected area increases with the number of pulses and laser intensity, e.g. 60 μ m was the diameter observed for 1 pulse at $2.5 \cdot 10^4$ watt/cm² as against about 100 μ m at $18 \cdot 10^4$ watt/cm². The affected area diameter increased from about 10 μ m to above 140 μ m for one and ten pulses at $18 \cdot 10^4$ watt/cm² respectively.

A treated area with better applicable morphology was achieved when the pulse energy density was $0.25 \cdot 10^9$ watt/cm². Higher energies produced undesirably deep craters in the Pb-Sn coating. This was the reason for choosing $0.25 \cdot 10^9$ watt/cm² as the working condition for treatment of large areas.

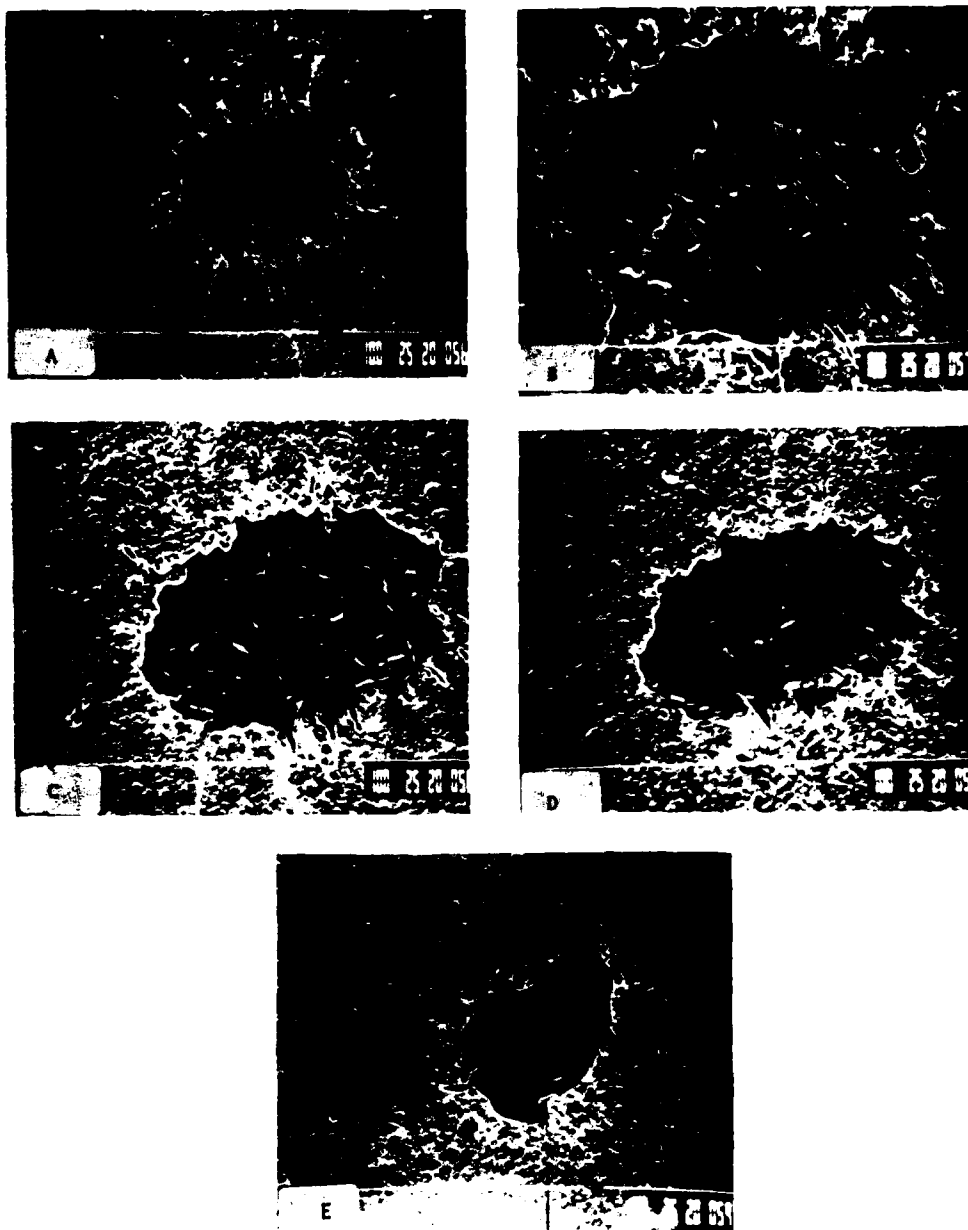


Fig. 4.21: SEM observations of single-pulse irradiation at various energy densities. Deposit thickness was $6\mu\text{m}$.

- A. $1.8 \cdot 10^9$ watt/cm², x350.
- B. $1.4 \cdot 10^9$ watt/cm², x750.
- C. $0.8 \cdot 10^9$ watt/cm², x750.
- D. $0.55 \cdot 10^9$ watt/cm², x750.
- E. $0.25 \cdot 10^9$ watt/cm², x750.

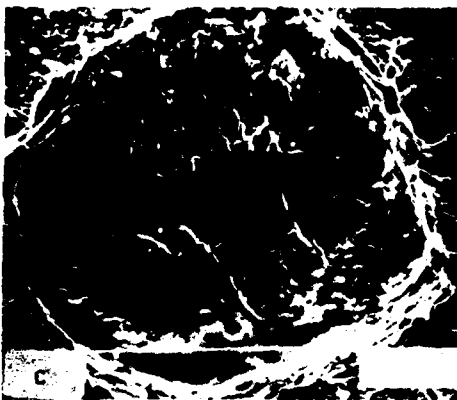
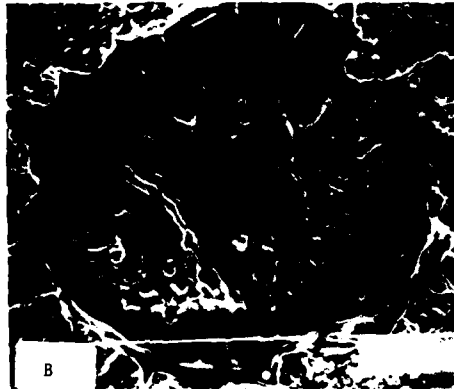
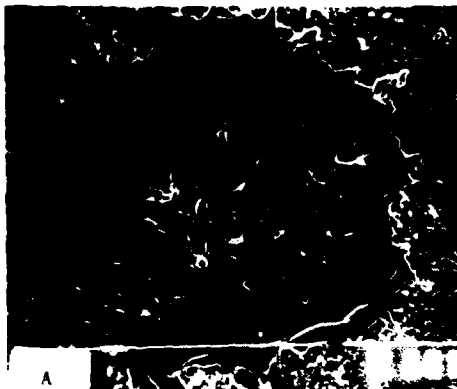


Fig. 4.22: SEM observations of the effect of number of pulses at constant pulse intensity. Laser energy per pulse $1.8 \cdot 10^9$ watt/cm². Deposit thickness 6.0 μ m.

- A. Two pulses, x750.
- B. Three pulses, x750.
- C. Five pulses, x750.
- D. Ten pulses, x750.

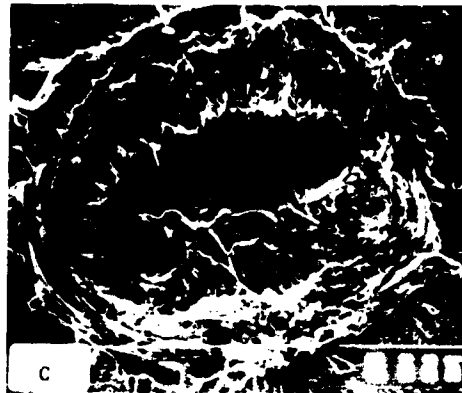
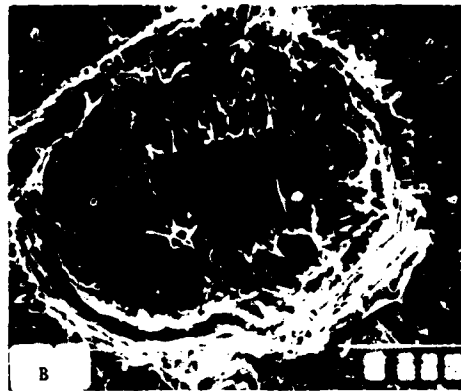


Fig. 4.23: SEM observations of effect of number of pulses at constant pulse intensities. Laser power per pulse $1.4 \cdot 10^9$ watt/cm².
 A. Two pulses.
 B. Five pulses.
 C. Ten pulses.

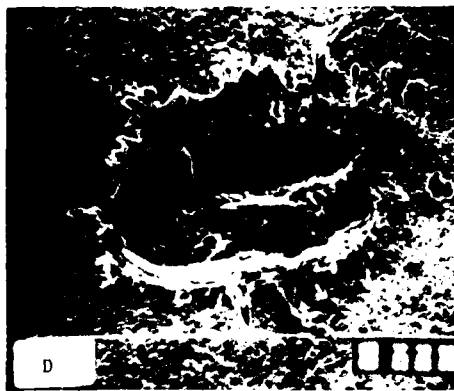
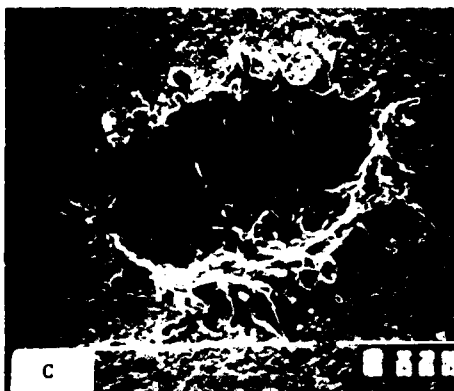
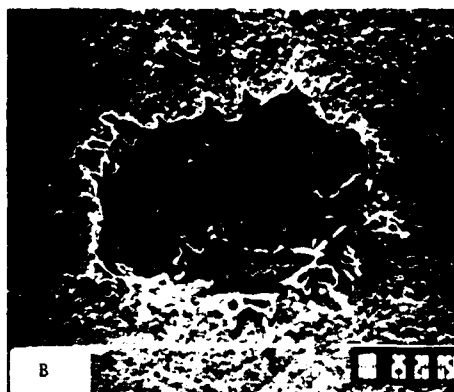
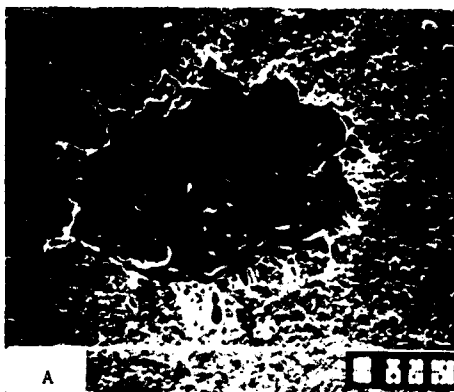


Fig. 4.24: SEM observation of effect of number of pulses at constant pulse intensity. Laser energy per pulse $0.55 \cdot 10^9$ watt/cm².
 A. Two pulses, x750.
 B. Three pulses, x750.
 C. Five pulses, x750.
 D. Ten pulses, x750.

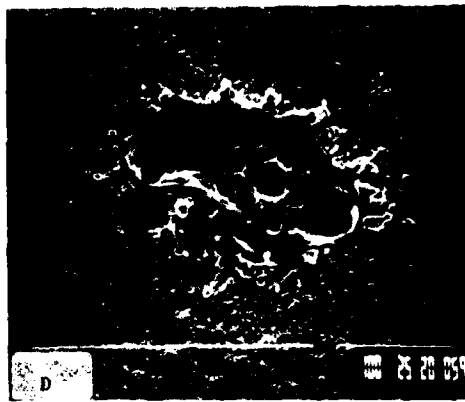
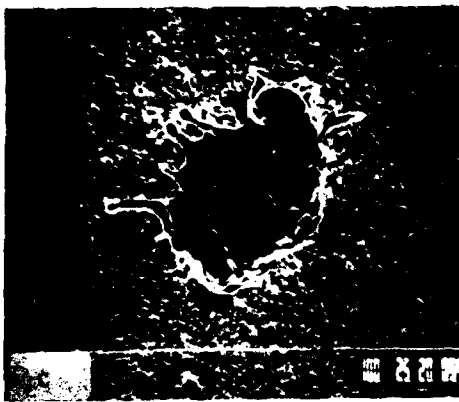
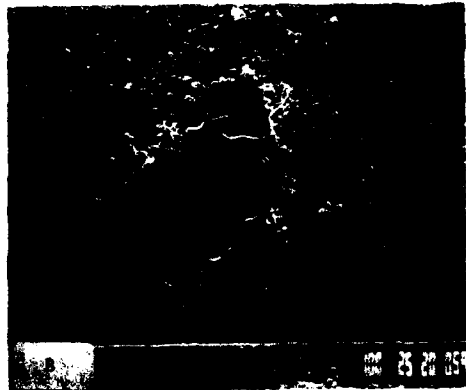
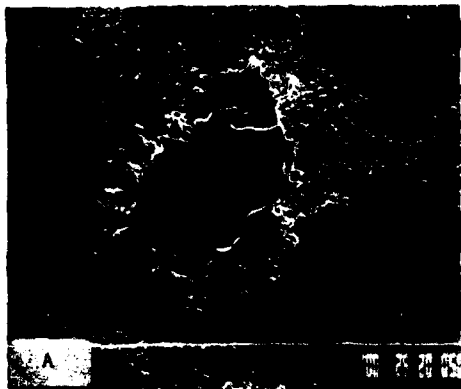


Fig. 4.25: SEM observations of effect of number of pulses,
laser energy per pulse 0.25 watt/cm^2 .
A. Two pulses, x750.
B. Three pulses, x750.
C. Five pulses, x750.
D. Ten pulses, x750.

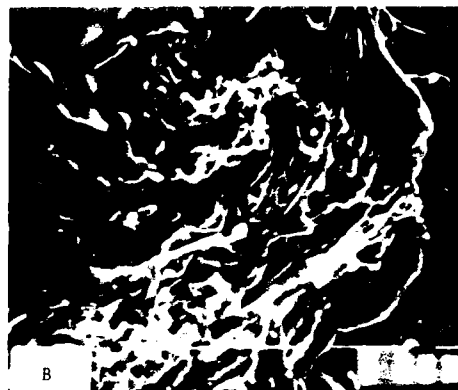


Fig. 4.26: SEM observations of effect of number of pulses and energy density. High magnification views.
 A. $1.8 \cdot 10^9$ watt/cm² one pulse, x3500.
 B. $1.8 \cdot 10^9$ watt/cm² ten pulses, x2000.
 C. $0.25 \cdot 10^9$ watt/cm² one pulse, x3500.
 D. $0.25 \cdot 10^9$ watt/cm² three pulses, x5000.

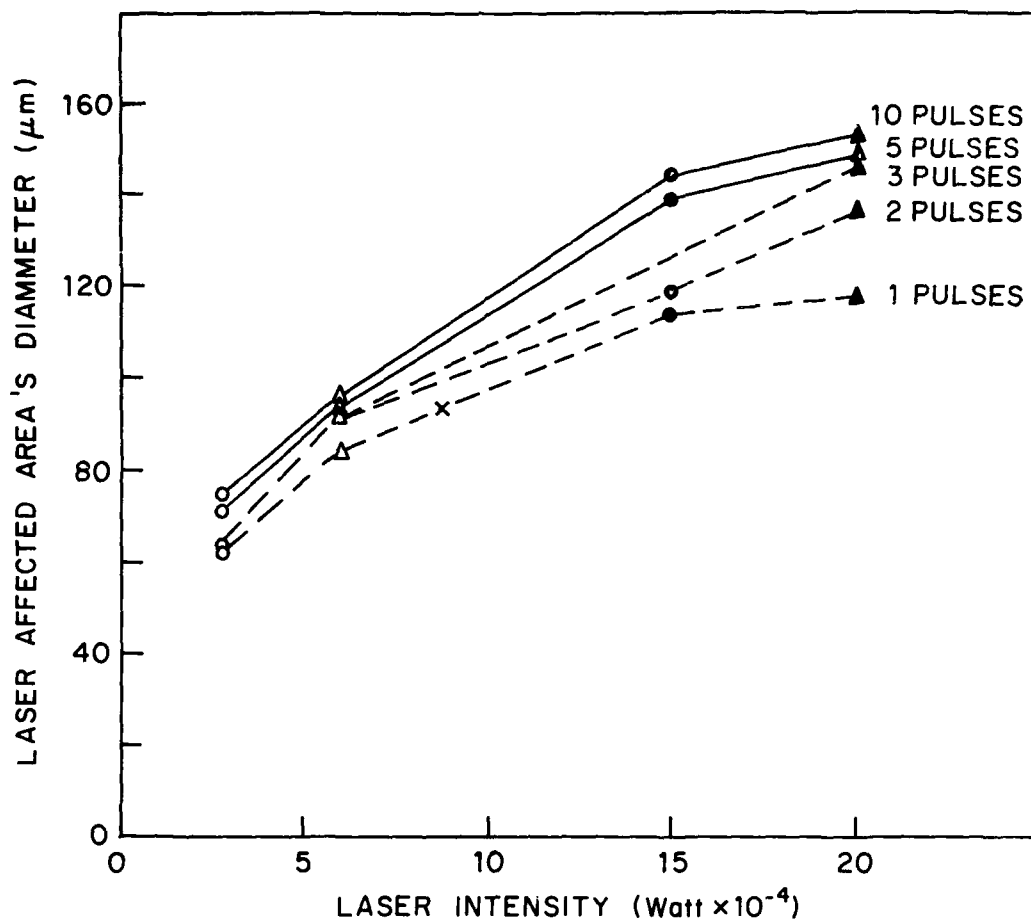


Fig. 4.27: Effect of laser intensity on affected area.

4.3.3 Laser Experiments - Area

Fig. 4.28 is SEM observation of the area produced by moving the specimen in overlapping lines by computerized x-y table, using the lowest pulse energy density - $0.25 \cdot 10^9$ watt/cm². Fig. 4.28a is a general view of the treated area, while Fig. 4.28b,c show the details of the area between the lines. The overlap between the pulses in each individual line was satisfactory and that between the lines almost complete. Fig. 4.28d shows the edge of the treated area and the difference between the melted zone and the background. Figs. 4.28e,f are higher magnifications of the treated area, showing the melted area with Pb-rich bright zones produced by the laser treatment.

Table 4.6 summarizes the E.D.S. results obtained in the above experiments. The untreated area composition was about 57% Pb and 42% Sn, while the treated area contained about 45% Pb and 51% Sn. Two causes can be offered for this phenomenon: 1) Volatilization of Pb as a result of the laser treatment; 2) Inhomogeneity of the melted zone. The composition of the bright zones was about 90% Pb and 9% Sn, while the area between contained approximately 16% Pb and 83% Sn.

Table 4.6: Summary of E.D.S. Results Obtained During Production of Laser Treatment Area On Pb-Sn Coating (Fig. 4.28 F)

	Pb Wt%	Sn Wt%	Cu Wt%
Background untreated area	57.5	41.8	0.69
Laser treated area	44.7	51.2	4.1
Bright zone in laser treated area	89.7	9	1.3
Between bright zones	16.2	82.6	1.2

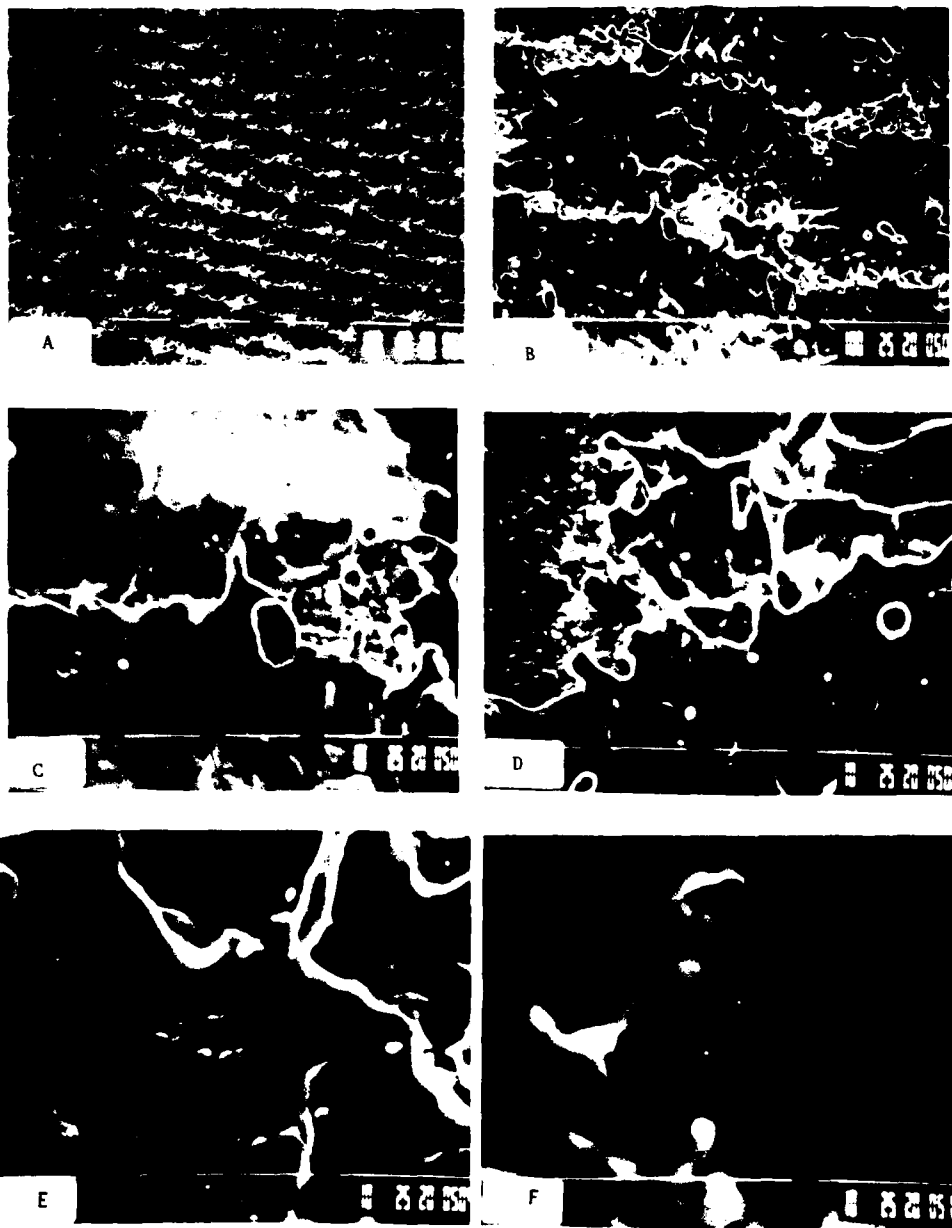


Fig. 4.28: SEM observations of area formed on 5.5 μm Pb-Sn coating of copper foil. Power density per pulse 0.25-10³ watt/cm². R.R. 2Hz, overlap 0.5, scan speed 25 $\mu\text{m}/\text{sec}$. Space between lines 50 μm .
 A. General view, x150.
 B. x750.
 C. Between lines, x2000.
 D. Edge area x2000.
 E. x3500
 F. x7500.

4.3.4 Laser Experiments - Defocusing

In order to minimize the unevenness of the treated surface experiments with defocusing of the laser beam were conducted (Figs. 4.29, 4.30). Fig. 4.29 shows the treated areas for the single, five and ten pulses variants. The affected areas had irregular shapes (created by laser beam cross-section and its reflected image) and differed from the untreated one by melting of the surface as can be seen clearly for ten pulses and a single pulse, respectively (Figs. 4.29c,d).

These Figs. also show that the effect intensified with the number of pulses.

A large area produced by overlapping between lines is shown in Fig. 4.30.

Fig. 4.30 is an overview of the treated area, while Figs. 4.30 b and c show it at higher magnifications. The difference in surface morphology between the treated and untreated variants is seen clearly in Fig. 4.30d; it is also confirmed by the E.D.S. analysis (Table 4.7), which indicates a transformed zone - bright spots with higher Pb concentration - the general composition of the area remaining as about 51% Pb, 41% Sn and 8% Cu.

These results seem to be promising and in this direction work will continue.

Table 4.7: E.D.S. Results of Various Areas Shown in Fig. 4.30

	Pb Wt%	Sn Wt%	Cu Wt%
Untreated	50.39	41.36	8.23
Bright spot (Point 1)	81.73	10.67	7.60
Between bright spots (Point 2)	81.19	81.34	10.41
Treated area overview	51.41	41.06	7.53

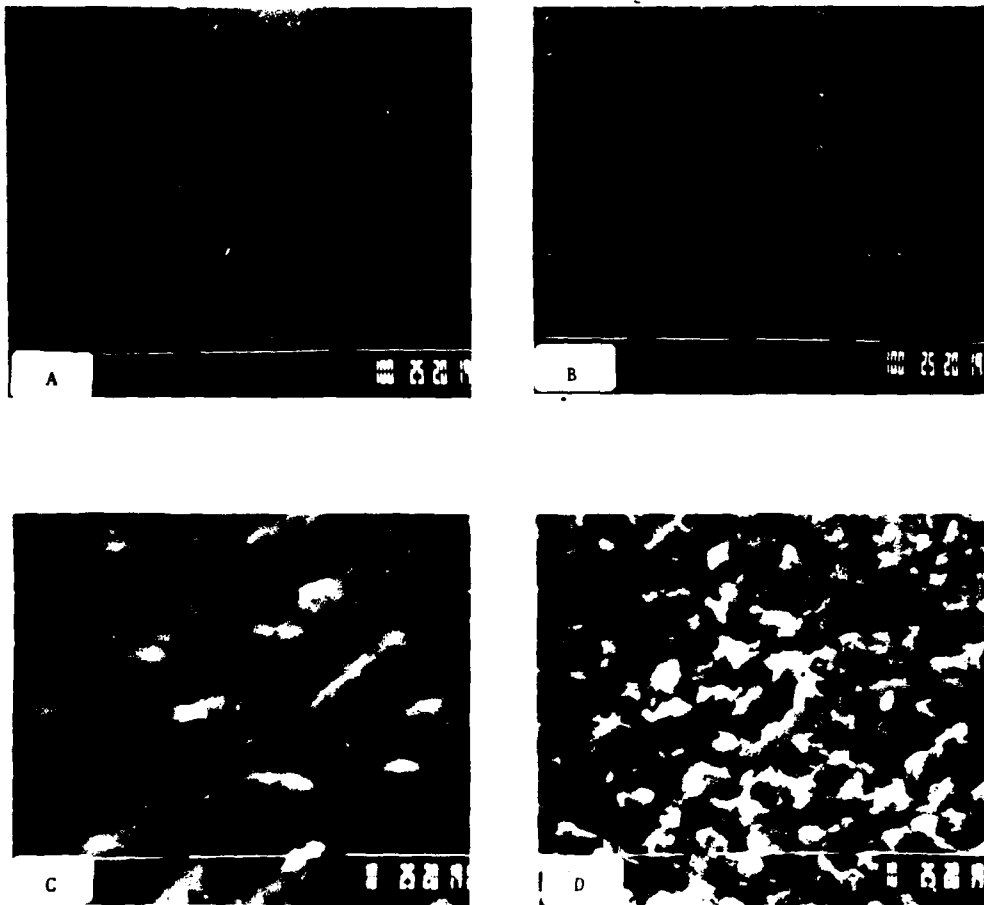


Fig. 4.29: SEM observations of defocusing experiment.
 Laser intensity 0.001 watt.
 A. One, five and ten pulses, x35.
 B. Ten pulses, x200.
 C. Ten pulses, x3500.
 D. Single pulse, x3500.

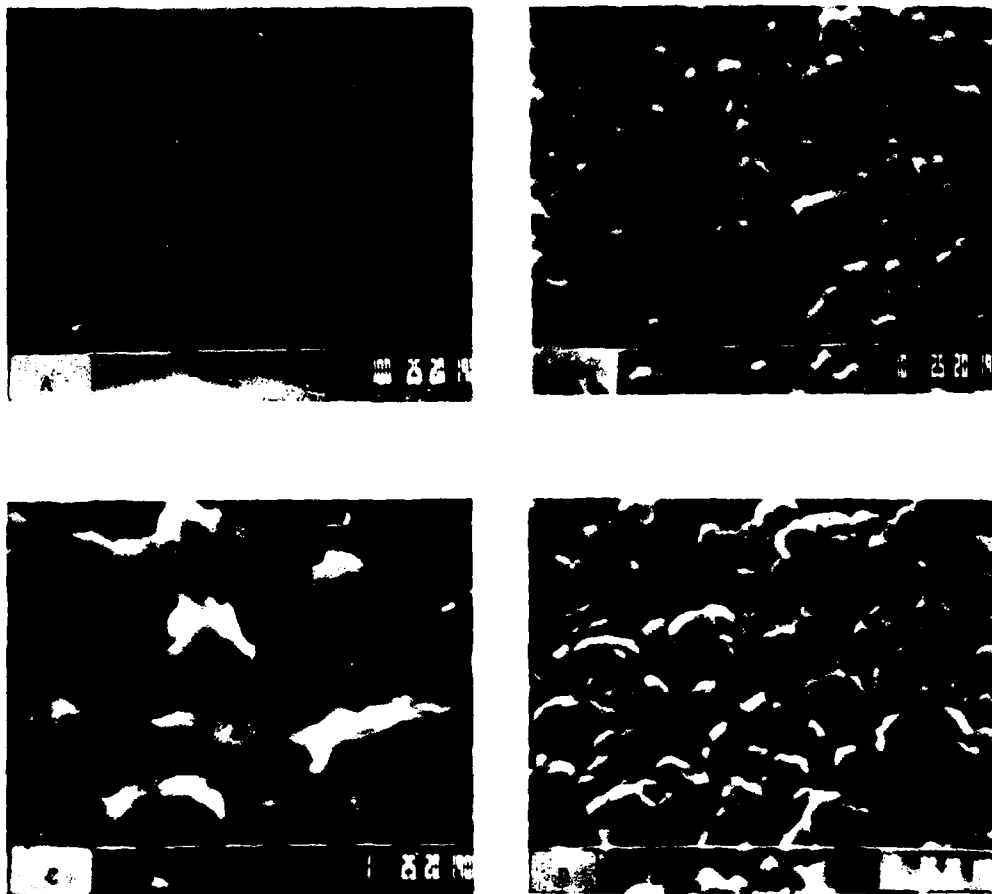


Fig. 4.30: SEM observation of defocusing laser experiment.
 Laser intensity 0.001 watt.
 A. General view, x35.
 B. Affected area x3500.
 C. Affected area, x10000.
 D. Area without laser treatment, x7500.

4.3.5 Auger Spectroscopy Observations of Laser Treated Area

In order to examine the surface of the melted area, Auger spectroscopy was used. Fig. 4.31 shows Auger observations of the untreated area and Fig. 4.32 those of the treated area. The specimen examined was the one in Fig. 4.28 where laser treated area was produced on 5.5 μm Pb-Sn coating. No significant difference was observed between the two areas. Tin oxide was observed on the outer surface and its content decreased as the sputtering proceeded inward. At 20A° deep Pb the content exceeded the Sn content while the oxygen content also decreased. The Pb content of the untreated area reached a maximum of 70% (A.C%) and decreased to about 60%; (that of the treated area reached a maximum of about 64% and decreased to about 52% at 200A° from the surface.

The main difference between the two areas was the lower Pb content of the as-received against treated areas (4% against 12% Pb (A.C%)) with the correspondingly lower tin and oxygen contents (40% against 30%). This effect is attributable to preferential volatilization.

4.3.6 X-Ray Diffraction

Fig. 4.33 shows the x-ray diffraction done on the Pb-Sn coating and Table 4.8 the peak intensities of the treated and untreated areas. Pure Pb, Sn and Cu were found, without any intermetallic compounds; the same peaks appeared for both areas, only their intensity varied. This is due to the fact that the basic crystalline structure was not affected by the treatment.

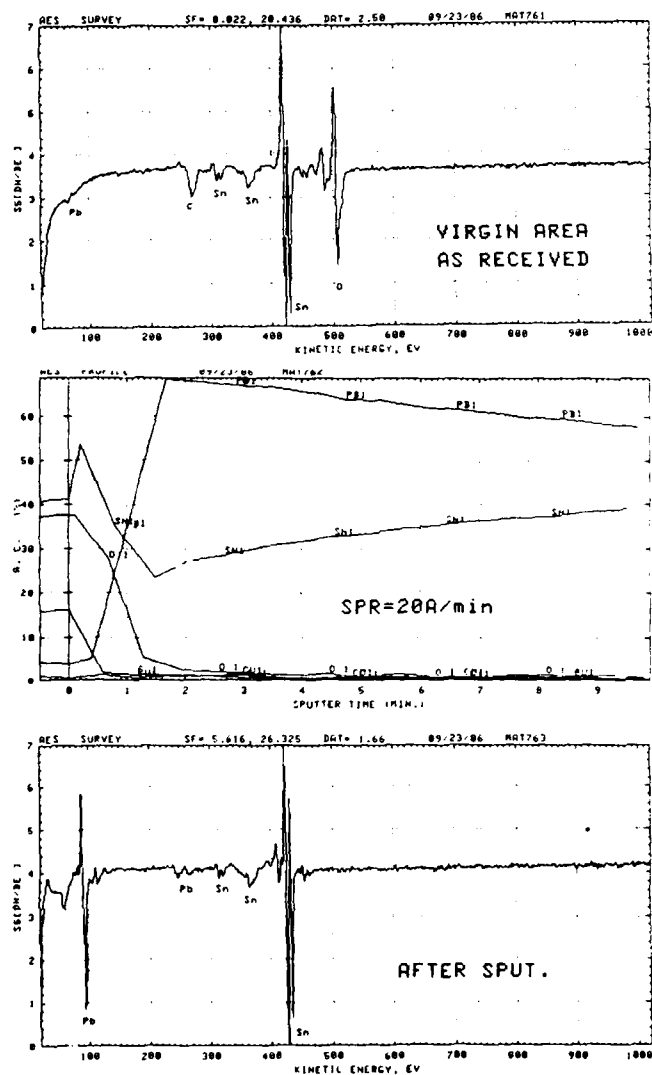


Fig. 4.31: Auger spectroscopy observations of Pb-Sn coating

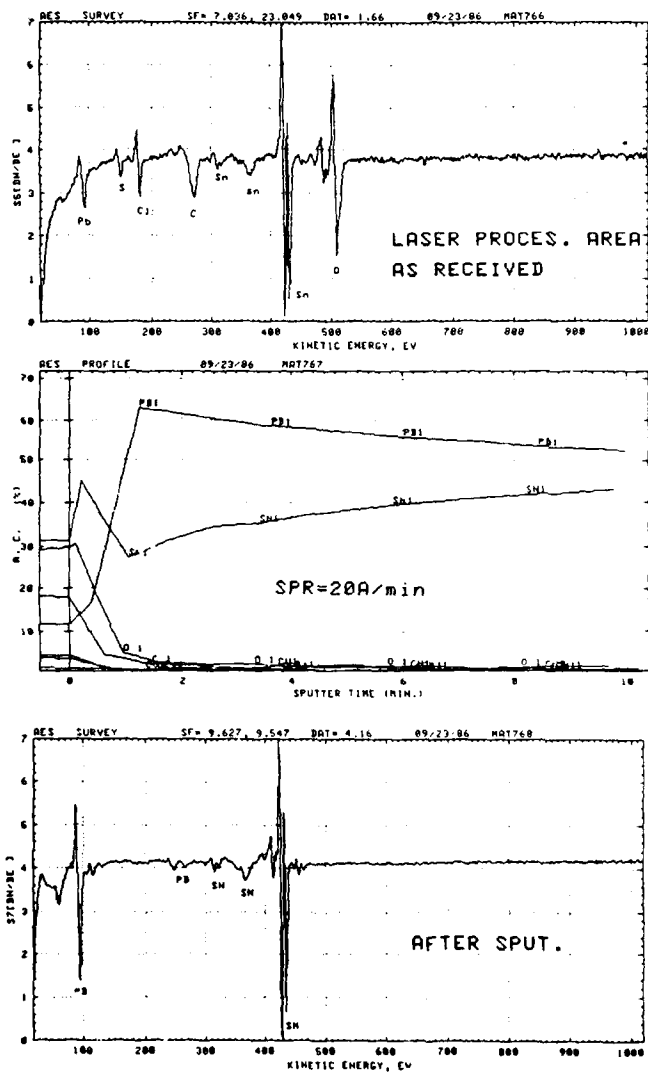


Fig. 4.32: Auger spectroscopy observations of laser treated area of Pb-Sn coating

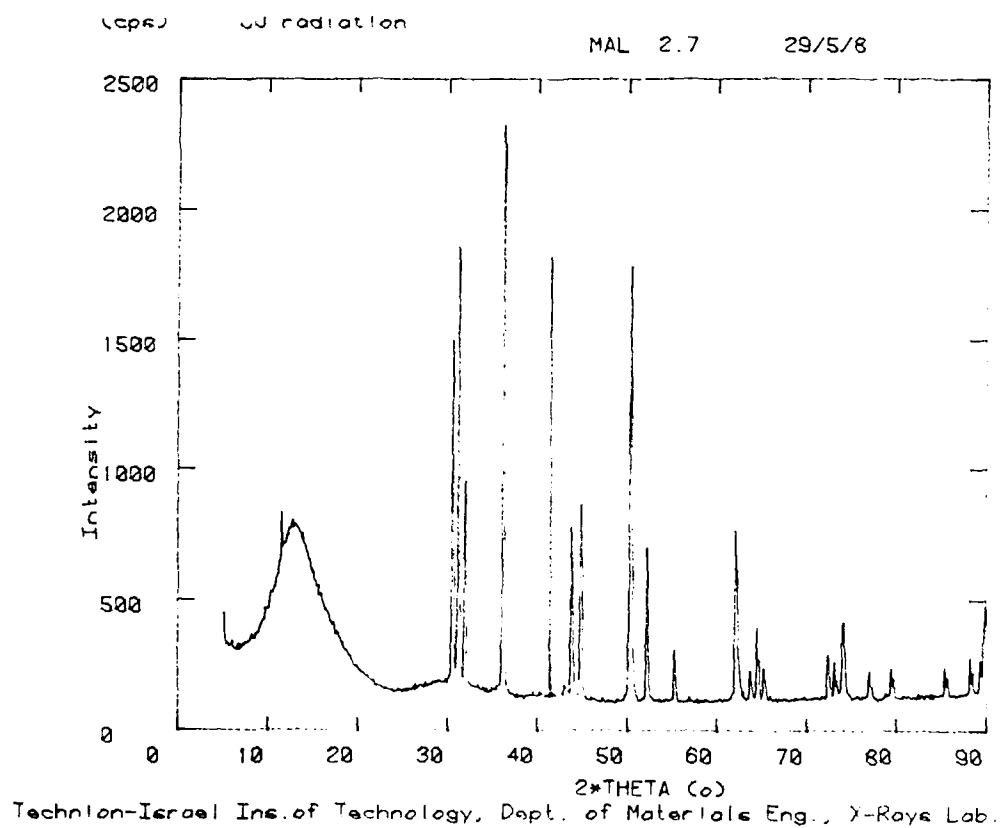


Fig. 4.33: X-ray diffraction of Pb-Sn coating
(2.7 μ m on copper foil)

Table 4.8 A. X-Ray Diffraction of Pb-Sn Coating (2.7 μ m on copper foil)

Interplanar spacings and intensities: MAL 2.7 29/5/86
X-ray target material: CO Wave length=0.15418nm
Reset time: 5sec. Increment 0.1 degree
Measurements taken for 2*Theta=5 to 90 degrees

#	Theta ($^{\circ}$)	2*Theta ($^{\circ}$)	Interplanar Spacing (n,m)	Peak Intensity
1	5.000	10.000	0.8845	21
2	5.800	11.600	0.7629	38
3	15.300	30.600	0.2922	67
4	15.600	31.200	0.2867	82
5	16.000	32.000	0.2797	43
6	18.150	36.300	0.2475	100
7				
8	21.500	43.000	0.2103	8
9	21.900	43.800	0.2067	35
10	22.450	44.900	0.2019	39
11	25.200	50.400	0.1811	80
12	26.100	52.200	0.1752	71
13	27.650	55.300	0.1661	14
14	31.050	62.100	0.1495	34
15	31.850	63.700	0.1461	11
16	32.250	64.500	0.1445	18
17	32.600	65.200	0.1431	11
18	36.200	72.400	0.1305	13
19	36.550	73.100	0.1295	12
20	37.050	74.100	0.1280	19
21	38.500	77.000	0.1238	10
22	39.700	79.400	0.1207	11
23	41.630	83.300	0.1175	6
24	42.700	85.400	0.1157	11
25	44.100	88.200	0.1108	13
26	44.650	89.300	0.1097	12

Table 4.8 B. Laser Treated Area X-Ray Diffraction

Interplanar spacings and intensities: MAL+LASER

2.7 1/6/86

X-ray target material: CO Wave length=0.15418nm

Reset time: 5sec. Increment 0.1 degree

Measurements taken for 2*Theta=5 to 90 degrees

#	Theta (°)	2*Theta (°)	Interplanar Spacing (nm)	Peak Intensity
1	15.300	30.600	0.2922	34
2	15.650	31.300	0.2858	71
3	16.000	32.000	0.2797	27
4	18.150	36.300	0.2475	72
5	21.550	43.100	0.2099	5
6	21.590	43.900	0.2062	22
7	22.450	44.900	0.2013	29
8	25.250	50.500	0.1807	100
9	26.150	52.300	0.1749	25
10	27.700	55.400	0.1658	8
11	28.900	57.800	0.1595	4
12	31.100	62.200	0.1492	27
13	31.900	63.800	0.1459	8
14	32.300	64.600	0.1443	12
15	32.650	65.300	0.1429	9
16	36.200	72.400	0.1305	10
17	36.600	73.200	0.1293	8
18	37.050	74.100	0.1280	20
19	38.550	77.100	0.1237	8
20	39.750	79.500	0.1206	10
21	42.750	85.500	0.1136	10
22	44.150	88.300	0.1107	10
23	44.700	89.400	0.1096	11

5. DISCUSSION

5.1 Corrosion of Pb-Sn Alloy Coating

Corrosion of the Pb-Sn alloy was studied by potentiodynamic polarization and the corroded specimens were examined by SEM. The Tafel calculations was used to determine the corrosion rate in MPY (milli-inch per year). The slightly acid aqueous chloride medium was chosen as a potential corrosion-inducing agent within the microelectronic process and the user environment.

As is seen from the background review, the composition of the Pb-Sn alloy is a significant consideration that has to be taken into account when the corrosion of the alloy is analysed.

5.1.1 Polarization Curves

Polarization curves obtained during the potentiodynamic scans were typically characteristic of the general corrosion type, without a passivation zone and without localized corrosion behavior (Figs. 4.1, 4.3-4.5). The curves obtained for the laboratory specimen differed from those obtained for the commercial specimen in some reduction of the current at the -0.5v potential followed by an immediate increase and possibly due to a change in the controlling corrosion reaction.

5.1.2 Effect of Chloride Concentration

Chloride concentration affected the corrosion rates obtained during potentiodynamic polarization. Fig. 4.2 showed that the highest corrosion rates were obtained when the chloride concentration was 0.025M with lower MPY values both above and below it. This behavior is seen also for the laboratory specimen. Corrosion rates obtained at 10^{-2} M Cl^- were higher than those obtained at 10^{-1} M Cl^- (Fig. 4.6, Tables 4.2, 4.3), in agreement with the observation that in potassium chloride the corrosion rate increases to a maximum in 0.05M solution, decreases with higher concentration, and increases again in 2M solution (Chap. 2.3.2). This effect may be due to the limited solubility of lead chloride: at low

AD-A181 963

LASER AND ELECTROCHEMICAL STUDIES OF METALLIZATIONS IN - 2/8

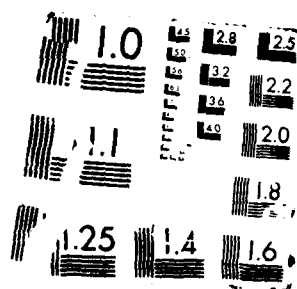
ELECTRONIC DEVICES (U) ISRAEL (NS) OF METALS HALTS

J ZAHUI ET AL. JAN 87 EOAD-IR-87-06 AFOSR-85-0309

UNCLASSIFIED

F/G 11/6.1 NL





concentrations of the medium the lead chloride is completely dissolved, up to a certain level beyond which an insoluble film is formed, inhibiting further dissolution.

5.1.3 Effect of Heat Treatment On Corrosion Resistance

Heat treatments considered during this year's project included: a commercial specimen preparation - reflow and heating in an oven. Laser treatment is also a heat treatment, but no corrosion tests were done during this year on laser treated areas.

The heat treated specimens have a smaller corrosion rates than the untreated ones (Fig. 4.6). This behavior is explained by transformation of the structure, as can be seen in Figs. 4.11, 4.12, and 4.14. The E.D.S. microanalysis shows that most of the Pb was dissolved during polarization of the as-deposited specimen. By contrast, the heat treated specimen lost only a third of the initial Pb concentration (Table 4.4, Figs. 4.13, 4.16). While in the corroded as-deposited area many very small grains disappeared during polarization (Fig. 4.12) only few were missing in the heat treated specimen (Figs. 4.14, 4.15). A possible explanation is the as-deposited specimen has two distinct kinds of grains rich in Pb and Sn respectively. Thus half of the Pb-containing grains are more anodic than the others and dissolve readily. The heat treatment in the oven caused a more uniform distribution of the α grains between the eutectic grains; the result was a negligible potential difference, and only one third of the Pb was dissolved.

The reflow specimen's corrosion rate was lower for most of the cases than that of the as-deposited specimen, but there is not enough data to establish a definite relationship. The laser treated specimens had a morphology similar to the reflow specimen, and their corrosion behavior is expected to be the same.

5.1.4 Effect of Coating Thickness on Corrosion Resistance

Increase in coating thickness caused improvement of corrosion resistance or decrease in corrosion rate (Fig. 4.6), attributable to the attendant reduction in porosity. For the thinner coatings, the cathodic action of the cathodic copper base was stronger and made for heavier dissolution of the

anodic coating. Lead has a more negative potential than tin, -0.4v as against -0.2v (vs. S.H.E.) (Fig. 2.12), so the lead-rich α solid solution dissolves first.

Thinly-coated ($2.8\text{ }\mu\text{m}$) specimens formed copper chloride during polarization, while none was found on those with the thicker coating (Figs. 4.12, 4.13, Table 4.4).

5.1.5 Corrosion Mode

Analysis of the corroded specimen by E.D.S. and SEM shows that Pb is preferentially dissolved during polarization (Table 4.13) at an anodic reaction site in the Pb-rich zone (α solid solution) while a cathodic reaction occurs in the tin-rich zone (β solid solution), as described in Fig. 5.1.

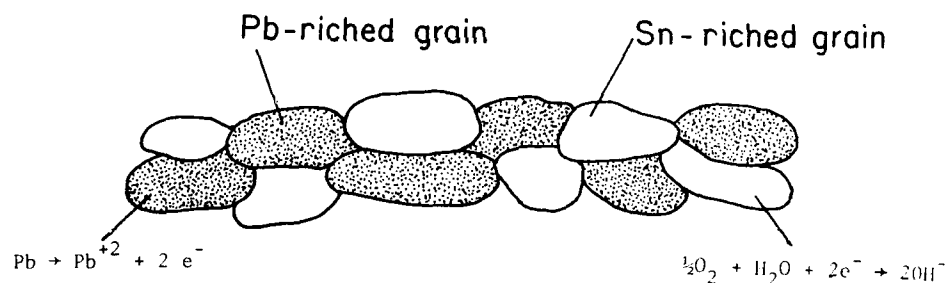


Fig. 5.1: schematic description of corrosion mode of Pb-Sn as-deposited specimen

Heat treatment in an oven causes more uniform distribution of Pb and Sn, thus reducing Pb dissolution and the corrosion rate.

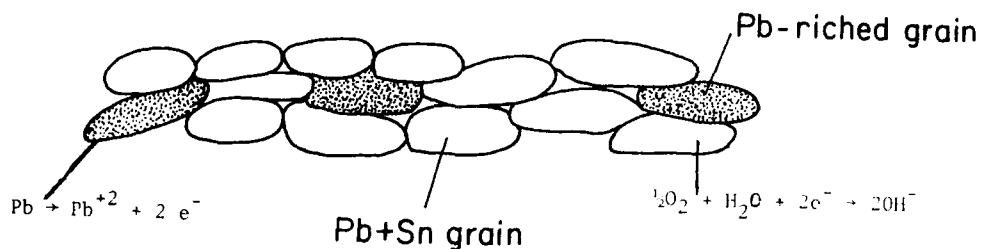


Fig. 5.2: Schematic description of corrosion mode of heat treated Pb-Sn alloy coating

The effect of laser treatment on the corrosion mode had to be studied. On the basis of the resulting structure, we can assume that formation of Pb-rich zones (Fig. 4.18) competes with other laser effects such as reduction of porosity or improved adhesion in determining the corrosion resistance.

5.2 Effect of Heat Treatment On Metallurgy of Pb-Sn Alloy Coating

The phase diagram of Pb-Sn (Fig. 2.2) contains, on both sides, solid solutions with limited solubility range α and β , rich in Pb and Sn respectively. The eutectic point is at 183°C, where the corresponding composition of α is 19.25 Sn and 80.85 Pb and that of β 97.55 Sn and 2.5% Pb. Starting with a liquid eutectic solution, the proportions of α and β at 183°C are 0.455 and 0.545 respectively (lever rule).

The commercial specimen (Chap. 4.2.1, Fig. 4.8) had as plated composition of 40% Sn and 60% Pb. The reflow specimen show bright zones with 10% Sn and 88% Pb with surrounding areas consisting of 32% Pb and 67% Sn. These bright zones may be α surrounded by eutectic.

In the laser treatment experiment (Chap. 4.33, Table 4.6), the untreated surface composition was 57%Pb and 42%Sn, while the bright zones of the treated surface consisted of 90%Pb and 9%Sn and the surrounding treated areas of 16%Pb and 83%Sn. Comparing this with the case of 60%Pb and 40%Sn

discussed before we see a difference in behavior by separation of Pb-rich zone (α grains) against a back ground of uneutectic Sn-rich composition. Understanding of the heat treatment of as-deposited surface with eutectic composition will be later investigated by laser treatment.

It is important to consider the non-equilibrium conditions of the heat treatments involved in these projects that cause the difference from phase diagram compositions: A) The short time of heating and the very rapid cooling rates that are in the range of ns in the case of laser treatment. B) Pb is heavier than Sn, and during solidification it tends to sink and produce regions with high Pb content.

5.3 Effect of Laser Treatment On Surface of Pb-Sn Alloy

Auger spectroscopy results shown in Chap. 4.3.5 are in agreement with those of Bird [8] and Frankenthal [9] reflecting a higher amount of tin oxide at the surface of the as-deposited Pb-Sn alloy and of laser treated area. The film of tin oxide is about 50Å. The tin oxide may be depleted from the bulk, producing Sn deficiency in the layer adjoining the oxide film.

The laser-treated area shows a higher Pb content than the as-deposited area which can be explained by Frankenthal's [9] finding that above 180°C Pb is segregated at the surface of the Pb-rich Pb-Sn alloy.

5.4 Selection of Laser Conditions

Experiments at various laser intensities revealed that the higher the intensity, the heavier the surface damage. In order to minimize it, the intensity must be as low as $2 \cdot 10^8$ watt/cm² (Fig. 4.19, 4.20). Also, at this intensity only a pulse or two impinge at a given point; a higher number of pulses causes formation of very deep craters (Figs. 4.21, 4.22, 4.23, 4.24).

Experiments under defocusing, which made for lower energy density at the target surface because of the increased target area, resulted in no damage at all but rather improved smoothness due to melting of the surface. On the basis of the energy needed to melt 0.5 μ m of Pb (Appendix A approximation) it was found that 10^7 watt/cm² had to be

invested, and further experiments will be done under defocusing with lower energy densities.

5.5 Further Research

In the light of the present interesting findings, further work is called for with a view to a complete picture and to better insight:

- (a) Electrochemical polarization of laser treated area, using SEM, Auger spectroscopy and x-ray diffraction.
- (b) Effect of defocusing laser conditions.
- (c) Effect of alloy compositions.
- (d) Cross-sections of the laser-treated area, with regard to formation of Cu-Sn intermetallic.
- (e) Examination of the solderability of the Pb-Sn alloy coating before and after laser treatment.

6. CONCLUSIONS

1. Laser-induced melting of Pb-Sn coating resulted in a brighter area than the untreated one.
2. Maximum energy of $1 \cdot 10^8$ watt/cm² had to be used in order to prevent damage during laser treatment.
3. Affected laser area increased with increase of laser energy.
4. Laser treatment produced lead-rich zone believed to be a solid solution grains.
5. Corrosion rate decreased with increase of Pb-Sn coating thickness.
6. Heat treatment resulted in decrease of corrosion rate.
7. Surface analysis showed higher content of Pb on laser treated surface. Treated and untreated areas showed presence of tin oxide in 50A^o surface layer.
8. More work has to be done in order to reach better understanding of the processes involved during laser treatment of the Pb-Sn alloy coating.

7. REFERENCES

1. "Corrosion Measurement System" Operating and Service Manual. EG&G. Princeton Applied Research.
2. Shreir: Corrosion. Lead and Lead Alloys, Chap. 4.3, p. 4.68 to 4.85. Newnes - Butterworths, 1976.
3. Shreir: Corrosion: Tin and Tin Alloys, p.4.141 to 4.149. Newnes - Butterworths, 1976.
4. A.A. Abdul Azim and M.M. Anwar. "Corrosion and Passivity of some Pb-Sn Alloys in Various Media". Corrosion Science 1969,9, p.193.
5. N.A. Fawzy, G.H. Sedhamed and A.A. Mohamed: "Corrosion Behavior of Pb-Sn Binary Alloys in Acid Solutions", Surface Technology 14 (1981), 257-264.
6. M.A. FAWZY, G.H. Sedhamed and A.A. Mohamed: "Corrosion of Pb-Sn Alloy - Alkaline Solutions", Surface Technology 15 (1982), 147-152.
7. Metal Handbook: "Microstructure of Lead and Lead Alloys", Vol. 8, Am. Soc. Met. 1984.
8. R.J. Bird: "Corrosion-Resistant Lead-Indium and Lead-Tin Alloys: Surface Studies by Photo-Electron Spectroscopy". Metal Science Journal 1973, Vol. 7, p. 109.
9. R.R. Frankenthal and O.J. Siconolfi, Summary Abstract: The Equilibrium Surface Composition of Two Solid, Single Phase Tin-Lead Alloys", J. Vac. Sci. Techn. 20(3), 1982.
10. N. Bloembergen, "Fundamentals of Laser-Solid Interactions" in "Applications of Lasers in Materials Processing", Proc. of Conference of American Society for Metals, Metals Park, Ohio, 1979.
11. S.S. Charschan, Editor: Lasers in Industry, Laser Institute of America, Western Electric Series, 1972.
12. J.M. Poate, G. Foti and D.C. Jacobson, Editors: "Surface Modification and Alloying, by Laser, Ion and Electron Beams", Plenum Press, New York, 1983.

APPENDIX A

For Cu: $\alpha = 10^{-6}$ cm at $= 0.5 \mu\text{m}$
 $R = 0.5$ cm at $= 0.5 \mu\text{m}$
 $c_v \rho = 3.85$
 $D = 0.99 \text{ cm}^2/\text{sec}$

According to equation p. 13 we can calculate the intensity and energy density required to heat a surface layer of Cu to 10^3C for pulse duration $t_p = 7 \cdot 10^{-9} \text{ sec}$.

$$(2Dt_p)^{1/2} = (2 \cdot 0.99 \cdot 7 \cdot 10^{-9})^{1/2} = 1.177 \cdot 10^{-4} \text{ cm}$$

$$I = \frac{DT \cdot c_v \rho (2dt_p)^{1/2}}{(1-R)t_p} = \frac{1083 \cdot 3.85 (2 \cdot 0.99 \cdot 7 \cdot 10^{-9})^{1/2}}{(1-0.5) \cdot 7 \cdot 10^{-9}} = 1.4 \cdot 10^8 \text{ watt/cm}^2$$

This approximation assumed that the thermal diffusion distance exceeds the penetration depth.

For Pb: $R=0.5$ cm at $\lambda=0.3$. α is unknown and its value has no relation to real data.

$c_v \rho = 0.136 \cdot$
 $D = 0.21$
 $T_M = 327$

$$I = \frac{327 \cdot 0.136 \cdot \rho (2 \cdot 0.21 \cdot 7 \cdot 10^{-9})^{1/2}}{0.5 \cdot 7 \cdot 10^{-9}} = \frac{44.5 \cdot \rho \cdot 0.5 \cdot 10^{-4}}{3.5 \cdot 10^{-9}} = 71.8 \cdot \rho \cdot 10^{-5} = 0.7 \cdot 10^7 \text{ watt/cm}^2$$

This calculation is intended for approximation of the energy needed for melting Pb by pulse laser. $0.7 \cdot 10^7 \text{ watt/cm}^2$ are needed to melt the Pb surface according to our assumption with a thermal diffusion distance of $0.5 \cdot 10^{-4}$ i.e., $0.5 \mu\text{m}$.

END

DATE
FILMED

7-87